Uptake and molecular impact of aluminum-containing nanomaterials on human intestinal caco-2 cells

Holger Sieg, Caroline Braeuning, Birgitta Maria Kunz, Hannes Daher,
Claudia Kästner, Benjamin-Christoph Krause, Thomas Meyer, Pégah Jalili,
Kevin Hogeveen, Linda Böhmert, et al.

Uptake and molecular impact of aluminum-containing nanomaterials on human intestinal Caco-2 cells

Holger Sieg[1], Caroline Braeuning[1], Birgitta Maria Kunz[1], Hannes Daher[1], Claudia Kästner[2], Benjamin-Christoph Krause[3], Thomas Meyer[4], Pégah Jalili[5], Kevin Hogeveen[5], Linda Böhmert[1], Dajana Lichtenstein[1], Agnès Burel[6], Soizic Chevance[7], Harald Jungnickel[3], Jutta Tentschert[3], Peter Laux[2], Albert Braeuning[1], Fabienne Gauffre[7], Valérie Fessard[5], Jan Meijer[8], Irina Estrela-Lopis[4], Andreas F. Thünemann[2], Andreas Luch[3], and Alfonso Lampen[1]

[1] German Federal Institute for Risk Assessment, Max-Dohrn-Straße 8-10, 10589 Berlin, Department of Food Safety

[2] German Federal Institute for Materials Research and Testing (BAM), Unter den Eichen 87, 12205 Berlin

[3] German Federal Institute for Risk Assessment, Max-Dohrn-Straße 8-10, 10589 Berlin, Department of Chemical and Product Safety

[4] Institute for Medical Physics and Biophysics, Leipzig University, Härtelstrasse 16-18, 04275 Leipzig, Germany

[5] ANSES, French Agency for Food, Environmental and Occupational Health and Safety, Fougères Laboratory, Toxicology of contaminants unit, 10B rue Claude Bourgelat, 35306, Fougères Cedex, France

[6] Univ Rennes, CNRS, Inserm, BIOSIT - UMS 3480, US_S 018, F-35000 Rennes, France

[7] Univ Rennes, CNRS, ISCR (Institut des Sciences Chimiques de Rennes) - UMR 6226, F-35000 Rennes, France

[8] Felix Bloch Institute for Solid State Physics, Leipzig University, Linnéstraße 5, 04103 Leipzig

E-Mail addresses:

Holger Sieg: holger.sieg@bfr.bund.de, Caroline Braeuning: caroline.braeuning@mdc-berlin.de, Birgitta Maria Kunz: birgitta.kunz@bfr.bund.de, Hannes Daher: hannes.daher@bfr.bund.de, Claudia Kästner: claudia.kaestner@bam.de, Benjamin-Christoph Krause: benjamin-christoph.krause@bfr.bund.de, Thomas Meyer: Thomas.Meyer@medizin.uni-leipzig.de, Pégah Jalili: pegah.jalili@anses.fr, Kevin Hogeveen: kevin.hogeveen@anses.fr, Linda Böhmert: linda.boehmert@bfr.bund.de, Dajana Lichtenstein: dajana.lichtenstein@bfr.bund.de, Agnès Burel: agnes.burel@univ-rennes1.fr, Soizic Chevance: soizic.chevance@univ-rennes1.fr, Harald Jungnickel: Harald.Jungnickel@bfr.bund.de, Jutta Tentschert: Jutta.Tentschert@bfr.bund.de, Peter Laux: Peter.Laux@bfr.bund.de, Albert Braeuning: Albert.Braeuning@bfr.bund.de, Fabienne Gauffre: fabienne.gauffre@univ-rennes1.fr, Valérie Fessard: Valerie.FESSARD@anses.fr, Jan Meijer: jan.meijer@uni-leipzig.de, Irina Estrela-Lopis: Irina.Estrela-Lopis@medizin.uni-leipzig.de, Andreas F. Thünemann: Andreas.Thuenemann@bam.de, Andreas Luch: Andreas.Luch@bfr.bund.de, Alfonso Lampen: Alfonso.Lampen@bfr.bund.de

Corresponding author:

Dr. Holger Sieg, German Federal Institute for Risk Assessment, Max-Dohrn-Straße 8-10, 10589 Berlin, Department of Food Safety, holger.sieg@bfr.bund.de

Uptake and molecular impact of aluminum-containing nanomaterials on human intestinal Caco-2 cells

Abstract

Aluminum (Al) is one of the most common elements in the earth crust and increasingly used in food, consumer products and packaging. Its hazard potential for humans is still not completely understood. Besides the metallic form, Al also exists as mineral, including the insoluble oxide, and in soluble ionic forms. Representatives of these three species, namely a metallic and an oxidic species of Al-containing nanoparticles and soluble aluminum chloride, were applied to human intestinal cell lines as models for the intestinal barrier. We characterized physicochemical particle parameters, protein corona composition, ion release and cellular uptake. Different *in vitro* assays were performed to determine potential effects and molecular modes of action related to the individual chemical species. For a deeper insight into signaling processes, microarray transcriptome analyses followed by bioinformatic data analysis were employed. The particulate Al species showed different solubility in biological media. Metallic Al nanoparticles released more ions than Al_2O_3 nanoparticles, while $AlCl_3$ showed a mixture of dissolved and agglomerated particulate entities in biological media. The protein corona composition differed between both nanoparticle species. Cellular uptake, investigated in transwell experiments, occurred predominantly in particulate form, whereas ionic Al was not taken up by intestinal cell lines. Transcellular transport was not observed. None of the Al species showed cytotoxic effects up to 200 µg Al/mL. The transcriptome analysis indicated mainly effects on oxidative stress pathways, xenobiotic metabolism and metal homeostasis. We have shown for the first time that intestinal cellular uptake of Al occurs preferably in the particle form, while toxicological effects appear to be ion-related.

Introduction

Aluminum (Al) is the most frequent metal in the earth crust and reaches the human gastrointestinal tract via oral uptake (Willhite et al., 2012). However, the majority of Al is bound in minerals and oxides and therefore unavailable for the biological cycle (Lote and Saunders, 1991). Nevertheless, a certain amount gets dissolved, promoted by industrial processes and acidification of the environment (Exley, 2003, Wagner, 1999). Chemical activity, gastrointestinal bioavailability and biochemical mode of action are dependent on the species and the surrounding media (Powell and Thompson, 1993, Exley, 2016). A fraction of the oral exposure to Al has particulate nature. Recently, Al-containing nanoparticles were found in food for the first time (Loeschner et al., 2017). After ingestion, Al species can change their physicochemical characteristics along the gastrointestinal tract. Previous results indicate a partial dissolution of Al in the acidic stomach environment and resorption in the proximal part of the duodenum (Froment et al., 1989a). Bioavailable Al gets mostly excreted via the kidney (95 %) and more slightly via bile (2 %) or is accumulated in bones and other organs (Yokel and McNamara, 1988). The resulting biochemical and toxicological consequences are still disputed (Willhite et al., 2014, Lidsky, 2014). Up to now, there is still a lack of knowledge concerning toxicological effects and the hazardous potential of Al, although it certainly plays a role in blood and bone diseases (Alfrey et al., 1976, Vick and Johnson, 1985, Lin et al., 2013). Some researchers see evidence for a link of Al exposure with breast cancer and neurodegenerative disorders (Darbre, 2009, Walton, 2014). The chemical mechanisms behind these effects have not been completely revealed yet. Some studies consider ionic Al to cause oxidative damages, with observation of reactive oxygen species, lipid peroxidation or mitochondrial dysfunction (Gutteridge et al., 1985, Fraga et al., 1990, Zatta et al., 2002). There are also indications for Al-induced apoptosis (Savory et al., 2003) and genotoxicity (Kumar et al., 2009) *in vivo*. Many publications, however, do not distinguish between the different chemical species of Al. Differences between the effects induced by ionic species and nanoparticles were already shown for nano-silver (Hsiao et al., 2015) and nano-copper (Semisch et al., 2014), so a similar investigation on nano-aluminum is required to fill the knowledge gap concerning toxicological effects caused by Al.

Chemical conversions like partial dissolution, agglomeration and *de novo* particle formation have been observed during the passage of Al species through artificial digestion with gastrointestinal fluids (Sieg et al., 2017). Therefore, it is crucial to compare different particulate and non-particulate species when regarding element-specific effects. In this study,

we chose 3 representative Al species including metallic Al^0 nanoparticles, mineralic Al_2O_3 nanoparticles and soluble $AlCl_3$. These species are already known to exhibit different physicochemical characteristics (Sieg et al., 2017). In this study, we determined physicochemical parameters like size distribution, ion release and protein corona of these particles in biological media.

Furthermore, we addressed the intestinal cellular uptake of these Al species as well as possible mode of actions in human intestinal cells, to fill the lack of information. Therefore, the well-established intestinal model of differentiated Caco-2 cells has been used (Fogh et al., 1977, Lampen et al., 2004). These cells can mimic the intestinal epithelium and so can be used for *in vitro* uptake experiments (Xia et al., 2017, Lichtenstein et al., 2017, Ye et al., 2017, Lichtenstein et al., 2016, Je et al., 2017). As an enhancement of the Caco-2 model, cocultures, which are simulating the intestinal mucus (Lesuffleur et al., 1990, Wen et al., 2013, Castiaux et al., 2016) and M-cells (Gullberg et al., 2000, des Rieux et al., 2007, Lichtenstein et al., 2015), have been established. Cellular uptake mechanisms can differ between nanoparticles and ionic species. Ions are often taken up by receptor-mediated transport (Rolfs and Hediger, 1999), but nanoparticles are described to be taken up in vesicles by "trojan horse" mechanisms (Hsiao et al., 2015, Semisch et al., 2014). In this work, the cellular uptake of the different Al species was investigated by several analytical and imaging methods like atomic absorption spectroscopy (AAS), transmission electron microscopy (TEM), ion beam microscopy (IBM) and time-of-flight secondary ion mass spectrometry (ToF-SIMS). Toxic effects were addressed with *in vitro* methods including a transcriptome analysis on regulatory functions and the measurement of multiple toxicological endpoints like cell viability, cellular impedance, GSH-levels, ATP-levels, mitochondrial membrane potential, apoptosis, necrosis, IL8-release and NFκB activation.

Materials and Methods

<u>Chemicals and nanoparticles</u>

Most chemicals were purchased from Sigma-Aldrich (Taufkirchen, Germany), Merck (Darmstadt, Germany), or Carl Roth (Karlsruhe, Germany) in the highest available purity. Nanomaterials (Al^0-core surface-passivated nanoparticles and γ-Al_2O_3 nanoparticles) were supplied by IoLiTec (Heilbronn, Germany). Al^0 nanoparticles were stored and weighted under an argon atmosphere. Both particle species were freshly dispersed according to the modified NanoGenoTOX protocol (dispersion in 0.05% BSA/water by ultrasonication with KE76 tip for 5'09'' with ~20% energy), BSA was supplied by Carl Roth (Albumin Fraction V, $\geq$98%) and $AlCl_3$ was supplied by Sigma-Aldrich (Hexahydrate, $\geq$97%).

<u>Cell cultures and transport studies</u>

Caco-2 cells and Raji B-lymphocytes were cultivated in DMEM High Glucose, 10 % FCS, 1% penicillin/streptomycin (GE Healthcare, Solingen, Germany). For cultivation of HT29-MTX, 1% non-essential amino acids (NEAA) was added. 5,000 Caco-2 cells were seeded into each well of 96-well plates. 1 million of cells were grown for microarray analysis per 75 cm² flask. In every format, medium was changed every 2-3 days for a differentiation time of 21 days. For the 12-well transwell system, 50,000 cells per well were seeded as previously described (Lichtenstein et al., 2015). For the mucus coculture, Caco-2 and HT29-MTX were cocultivated (40,000/10,000 cells) in HT29-MTX medium. For the M-cell-model, transwell inserts were inverted into boxes 7 days after seeding. At day 16, 50,000 Raji cells were added from the basolateral side onto the inverted monolayer using a tube. At day 20, inserts were re-inverted back into the transwell system and incubated with samples 1 day later. For testing monolayer integrity, transepithelial resistance (TEER) values were determined and 1 mg/ml FITC-Dextran was used for measuring the passage into the basolateral compartment with a TECAN Infinite F200 Plate reader (Tecan, Switzerland). TEER values above 800 Ωcm² and p_{App}-values for FITC-Dextran below 10^{-6} were defined as indicators of good monolayer stability.

For the transport studies on the 3 coculture models, 500 µL medium containing 100 µg Al/ml or control medium were added to the apical compartment of the transwell and incubated for 24 h. Basolateral and apical compartments were collected and the monolayer was washed with 500 µl PBS. After washing, the membrane was cut out and all collected compartments

were digested by 69 % nitric acid microwave digestion using an MLS Ethos-1600 high pressure microwave (MLS, Germany) according to a previously described protocol (Lichtenstein et al., 2015). 4 independent experiments were performed in triplicates. The Al-content was determined by AAS comparable to previous studies (Lichtenstein et al., 2016).

Small-angle X-ray scattering (SAXS)

SAXS measurements were conducted in a flow-through capillary with a Kratky-type instrument (SAXSess from Anton Paar AG, Graz, Austria) at 21±1 °C. The SAXSess has a low sample-detector-distance of 0.309 m which is appropriate for the investigation of dispersions with low scattering intensities. The experiments were performed with 120 measurement cycles (each averaged over 10 s). The measurements were background-corrected with the respective mixture of aqueous BSA solution without addition of aluminum species. Deconvolution (slit length desmearing) of the SAXS curves was performed with the SAXS-Quant software (Anton Paar AG). Samples analyzed with SAXS were used as prepared. Curve fitting was performed with the software McSAS (Monte Carlo method, version 1.0.1). This procedure was described before (Kästner and Thünemann, 2016).

Ion release measurements

Al species were incubated at 2 concentrations, 4 and 100 µg Al/mL. Aliquots were taken in duplicates after 0, 3, 23 and 47 h. Ion release of nanoparticles in serum-containing cell culture medium (DMEM high glucose, 10% FCS, 1% P/S) was determined by ultracentrifugation (100,000 x g for 1 h at 4 °C) followed up by acidic hydrolysis of the supernatant (69% HNO_3, 180 °C for 20 min in an MLS-ETHOS Microwave system) and element analysis with AAS (Perkin Elmer AAnalyst 800, Shelton, USA) comparable to previous studies (Lichtenstein et al., 2016). Results are given as percentage of the initially used aluminum amount. Results are shown as mean values of 3 independent experiments with standard deviations and statistical analysis was performed with student's t-test indicated by asterisks (* $p<0.05$;** $p<0.01$; *** $p<0.001$).

Protein Corona Analysis

The Protein coronae were determined after 24 h incubation (37 °C, 5 % CO_2) of 100 µg Al/mL samples in serum-containing cell culture medium (CCM). Centrifugation was

performed in a Beckman Optima L centrifuge (Beckman, Unterschleissheim, Germany) for 1 h at 48,250 x g. Supernatants were removed, pellets suspended in 10 mL 50 mM sodium bicarbonate and transferred into a fresh tube. This washing step was repeated 3 times before, in the last step, the pellet was resuspended in 1 mL and centrifuged for 1 h at 153,700 x g. With these pellets, 2D-SDS-PAGE was performed as described before (Oberemm et al., 2009, Oberemm et al., 2016). Isoelectric focusing occurred according to a published protocol with 7 M urea and a 2 M thiourea-containing lysis buffer. After a second dimension migration (SDS-PAGE), gels were stained with ruthenium and photographed using a VersaDoc imager (VersaDoc MP 4000, BioRad, USA, excitation 450 nm, emission 605 nm). Spots were picked by self-made SpotXpress Spotpicker and digested by tryptic digestion over night for MALDI-TOF protein identification (Bruker Ultraflex II, Bruker, Berlin, Germany). Semi-quantitative data evaluation was carried out by manually comparing 4 replicates per sample using a VersaDoc imager.

Transmission Electron Microscopy (TEM)

Following a 24 h treatment with NMs, cells were rinsed twice with PBS and with 0.15 M Na cacodylate buffer (pH 7.2) before fixation by dropwise addition of glutaraldehyde (2.5%) for 45 min. The cells were rinsed several times with 0.15 M Na cacodylate buffer and post fixed with 1% osmium tetroxide for 45 min. After further rinsing with cacodylate buffer, the samples were dehydrated through an ethanol gradient from 70% to 100% and infiltrated in a mixture of acetone-epon resin (50/50) for 3 h, then, in pure epon resin for 16 h. Finally, the samples were embedded in DMP30-epon for 24 h at 60°C. Ultra-thin sections (90 nm) were cut on a Leica UC7 ultracut, collected onto copper grids and double-stained with 4% uranyl acetate and then with lead citrate (Reynold solution). Examination was performed with JEOL 1400 electron microscope operated at 120 kV equipped with a 2k-2k camera from Gatan Orius 1000 (MRic-TEM platform, Biosit, Rennes).

Time of flight secondary ion mass spectrometry (ToF-SIMS)

ToF-SIMS depth profiles were acquired using a ToF-SIMS V instrument (ION-TOF GmbH, Münster, Germany) with a 30 keV nano-bismuth primary ion beam source (Bi)x(y+)-cluster ion source with a BiMn emitter. The ion currents were 0.5 pA at 5 kHz using a Faraday cup. A pulse of 0.7 ns from the bunching system resulted in a mass resolution that usually exceeded 9,000 (full width at half-maximum) at m/z < 500 in positive ion mode. The primary

ion dose was controlled below 10^{12} ions cm^{-2} to ensure static SIMS conditions. Charge compensation on the sample was obtained by a pulsed electron flood gun with 20 eV electrons. The primary ion gun scanned a field of view of 200x200 µm applying a 512×512 pixel measurement raster. Once the primary ion gun was aligned, a ToF-SIMS mass spectrum was generated by summing the detected secondary ion intensities and plotting them against the mass channels. The analytical methodology was described in detail elsewhere (Booth et al., 2015, Tentschert et al., 2013, Haase et al., 2011, Jungnickel et al., 2005, Thompson et al., 2004). All depth profiles were performed in dual beam mode on a ToF-SIMS V instrument (ION-TOF GmbH, Münster, Germany) of the reflectron-type, equipped with a 30 keV bismuth liquid metal ion gun (LMIG) as primary ion source, a 20 keV argon gas cluster ion source both mounted at 45° with respect to the sample surface and an electron flood gun. Bi^{3+} was selected as primary ion by appropriate mass filter settings. Primary and sputter ion currents were directly determined at 200 µs cycle time (i.e. a repetition rate of 5.0 kHz) using a Faraday cup located on a grounded sample holder. Scanning area for analysis was 200 × 200 µm² with 512 × 512 pixels. The sputter area for each measurement was 1,000 µm x 1,000 µm. Surface charging was compensated by flooding with low energy electrons. ToF-SIMS depth profiles were acquired in positive ion mode. The mass scale was internally calibrated using a number of well-defined and easily assignable secondary ions ($C_2H_5^+$, $C_3H_7^+$ and $C_4H_9^+$) keeping the error in calibration for all spectra below 5 ppm. The data were evaluated using the Surface Lab software (ION-TOF GmbH, Münster, Germany).

Ion Beam Microscopy (IBM)

IBM measurements were performed at the LIPSION nanoprobe. A proton beam with an energy of 2.25 MeV was applied by a singletron accelerator. To minimize interactions between gas molecules and projectiles from the beam a vacuum with a pressure of 5.0 x 10^{-5} to 10^{-7} Torr was used. Micro-particle induced x-ray emission (µPIXE) element maps were recorded using a Canberra (Canberra, Connecticut, U.S.A.) PIXE detector consisting of a High Purity Germanium crystal with an area of 95 mm². To avoid interactions between the detector and backscattered protons the detector was shielded by a 60 µm polyethylene foil. For cellular analysis areas of 50 x 50 µm² were scanned. µPIXE was used to visualize two-dimensional distributions of aluminum, phosphorus and sulfur. GeoPIXE 5.1 (CSIRO Exploration and Mining, Victoria, Australia) was used for data analysis.

Cytotoxicity Assays

Cell viability was determined by the Cell Titer Blue assay (CTB, Promega, USA) followed by the MTT assay. Differentiated Caco-2 cells were incubated with 200 µL of different concentrations of Al species for 24 h and 48 h in 96-well-plates. After incubation time, 100 µL of the media was removed and 40 µL CTB reagent was added to the cells. After 20-30 min, fluorescence was determined with a Tecan plate reader (Ex. 560, Em. 590 nm). Next, 10 µL 5 mg/ml 3-(4,5-Dimethylthiazol-2-yl)-2,5-diphenyltetrazolium bromide (MTT) in PBS was added for another 1 h. After that, whole media was removed and 130 µL pre-warmed desorption agent (0.7 % w/v SDS in isopropanol) was added. Plates were shaken for 30 min and absorption was measured by a plate reader (570 nm) with subtraction of the background absorption (630 nm). Results were normalized on untreated controls after subtraction of equally treated cell free reference wells. As a positive control, 0.01% Triton X-100 was used. Statistics were performed as Student's t-test indicated by asterisks (* $p < 0.05$;** $p < 0.01$; *** $p < 0.001$).

Cellular impedance was determined by an xCELLigence system (xCELLigence, Roche, Germany). Caco-2 cells were differentiated in gold-coated 96-well E-plates, incubated with 200 µL testing substances and controls and measured over a time period of 48 h. The cell index was determined as mean values of at least 3 replicates with standard deviation. Cell indices were double-normalized to time point 0 and untreated controls. As a positive control, ZnO-Particles (IoLiTec, Heilbronn, Germany) were used.

Apoptosis / Necrosis measurements

Apoptosis / Necrosis measurements and cell cycle analysis were performed by flow cytometry with BD Accuri C6 (Accuri, Belgium). Caco-2 cells were cultivated and incubated as described before. After incubation, media were saved and cells were washed with 100 µl PBS, harvested with 50 µL trypsin/EDTA and collected in 200 µL warm, serum-containing CCM. Cells and media were reunited for each sample and centrifuged (3 min, 200 x g) to sediment the cells. Cells were washed with 800 µL cold PBS and then 800 µL annexin buffer afterwards (5 mM Hepes, 70 mM NaCl, 2.5 mM CaCl$_2$, pH 7.4). After that, cells were stained with AnnexinV-FITC (1:20) and 7AAD (1:10) at the same time in annexin buffer for 30 min. Fluorescence was detected for FITC (Ex. 488, Em. 533/30 nm) and 7AAD (Ex. 488, Em. >670 nm) and data for 10,000 cells each sample was collected. Color compensation was performed to avoid interactions between both fluorophores. Background level was determined

by untreated stained controls. Cells that were AxV-positive were defined as apoptotic; cells that were 7AAD-positive or double-positive were defined as late-apoptotic / necrotic. The relative cell counts of the populations were averaged over at least 3 independent experiments, error bars indicate standard deviations. Statistics were performed as student's t-test indicated by asterisks (* $p<0.05$;** $p<0.01$; *** $p<0.001$). As positive controls, 2 µM staurosporine (apoptosis) and 50 µM tert-butyl-hydroxyperoxide (tBOOH, necrosis) were used.

Transcriptome analysis

Caco-2 cells were grown and differentiated in 75 cm² cell culture flasks incubated for 24 h with different species and concentrations of Al by adding 1 mL of Al-containing nanoparticles and controls into 19 mL cell culture medium up to non-toxic final concentrations of 5, 25 and 50 µg Al/mL. Each condition was run in triplicates. After incubation, cell pellets were harvested by scraping into 1 mL PBS and cells were washed twice. Cell pellets were stored at -80 °C before use. RNA isolation was performed according to RNeasy Midi Prep kit (Qiagen, Germany) and the RNA amount was measured using a NanoDrop spectrophotometer. For the microarrays, only the highest exposure conditions of each Al-species were chosen, while the qPCRs were performed with all available conditions to gain information on the concentration dependency of the effects. 100 ng RNA of each sample was sent to Eurofins (Eurofins, Denmark) for microarray analysis using the human transcriptome array HTA 2.0. Data was analyzed by Affymetrix TAC 2.0 software (Affymetrix, UK) using as cutoffs a │fold change│≥ 1.5 and a one way ANOVA p-value <0.05. P-values were calculated automatically by the TAC 2.0 software according to the manufacturer's standard settings for microarray evaluation. Genes were only considered when they were significantly regulated, compared to the medium controls, in all 3 out of 3 technical replicates. Data evaluation was done using the software VennDis (Kisslinger Laboratories, Canada), Ingenuity Pathway Analysis (IPA, Qiagen, Germany) and geneontology.org (GeneOntology consortium, USA). Selected microarray results were verified by quantitative real-time PCR (qPCR, Applied Biosystems 7900 HT, Thermo Fisher Scientific, Berlin). The qPCRs were performed in technical triplicates; data evaluation was performed according to a standard protocol with representative deregulated genes of different sample groups using the ΔΔcT method referring to the housekeeping gene (GAPDH) and untreated control samples, as previously described (Buhrke et al., 2017). The ΔΔcT values for each condition were

averaged, marked with standard deviations and statistics were performed as Student's t-test indicated by asterisks (* $p<0.05$;** $p<0.01$; *** $p<0.001$).

Cellular Effects

Cellular effects were determined in 96-well-plates with differentiated Caco-2 cells as described before.

For GSH-levels, after incubation with substances and controls, the medium was removed prior to a 20-30 min incubation with 250 µL 40 µM monochlorobimane (MCB) in PBS. After that, cells were washed with 250 µL PBS and incubated with 150 µL desorption agent (see above) and shaken for 30 min. Fluorescence was measured with a plate reader (Ex. 380 nm, Em. 460 nm). Mean values were determined as described above. 100 µM buthioninesulfoximine was used as positive control.

Mitochondrial depolarization was determined by JC1 assay. Caco-2 cells were grown, differentiated and incubated as described before. After incubation, incubation media were removed and 100 µL 1 mg/ml JC1 in PBS was added for 20 min. After that, cells were washed twice with 250 µl PBS and finally 100 µL PBS were added for fluorescence measurements (Green: Ex. 485 nm, Em. 535 nm, Red: Ex. 535 nm, Em. 595 nm). Fluorescence ratio (Red / Green) was determined and mean values were normalized to untreated controls. As a positive control, 1 mg/mL valinomycin was used and added 2 h before the end of incubation time.

Relative ATP content was determined by Cell Titer Glo assay (Promega, USA) according to a standard protocol. Medium was removed except 100 µL per well. Following, 100 µL of ready-to-use reagent were added and shaken for 10 min. Luminescence was quantified for 1 second measuring time Mean values were determined as described before. A previously determined substance specific correction factor was taken into account to identify treatment-specific effects and to eliminate assay interactions (Lehmann et al., 2016). As positive control, 1 µM oligomycine was used. Statistics were performed as Student's t-test indicated by asterisks (* $p<0.05$;** $p<0.01$; *** $p<0.001$).

IL-8 release from cell via ELISA assay

The levels of interleukin-8 (IL-8) in cell media were measured using an enzyme-linked immunosorbent assay (ELISA). Primary IL-8 antibody (M801), biotin-conjugated human IL-

8 (M802B), recombinant IL-8 cytokine, HRP-Conjugated Streptavidin (N100), SuperBlock blocking buffer, 3,3',5,5'-tetramethylbenzidine (TMB), Tumor necrosis Factor alpha (TNF-α) and Tween 20 were obtained from Thermofisher scientific. 20 ng/mL Tumor necrosis Factor alpha (TNF-α) was used as positive control. Following 24 h incubation with particles, media were collected and frozen at 20 °C until analysis. 96 well microplates (Nunc) were coated with human recombinant IL-8 primary antibodies at 1 µg/mL and incubated overnight at 4 °C. Between each step, wells were washed with PBS-Tween 20 (0.05%). After saturation with SuperBlock for 1 h, samples and standards were added into the wells and incubated at room temperature for 2 h. Biotin-conjugated human IL-8 antibodies (0.1 µg/ml) were then added for 1 h followed by 100 µL of HRP 1:10,000 labeling for 45 min. Finally 100 µL of the chromogenic substrate TMB was added and the reaction was stopped with 100 µL of H_2SO_4 (1 M). Plates were read at 405 nm. The concentrations of IL-8 expressed in fold of negative control were calculated against a standard curve prepared in duplicate.

NFKB via High Content Screening (HCS)

The primary and secondary antibodies were purchased from Abcam (Cambridge, UK): rabbit monoclonal anti NFKB (ab16502), and goat anti-rabbit IgG H&L Alexia Fluor 647 (ab150079), prepared in blocking solution and filtered with a 0.2 µm syringe filter. After 1, 3 and 6 hours of treatment, cells were fixed with 4 % paraformaldehyde in PBS for 10 min and permeabilized with 0.2 % Triton X-100. Plates were then incubated in a blocking solution (PBS with 1% BSA and 0.05 % Tween-20) for 30 min before addition of the primary antibody (1/1000) overnight at 4 °C. . After 3 washes with PBS + 0.05 % Tween20, the secondary antibody (1/1000) was incubated for 45 min at room temperature. After two washes with PBS 1%, nuclear DAPI (1 µg/mL− 1) staining was used for automated cell identification by HCA.

Plates were scanned with the Thermo Scientific ArrayScan VTI HCS Reader (Thermo Scientific, Waltham, USA) and analyzed using the target activation module of the BioApplication software. For each well, 7 fields (20×magnification, white bar = 100 µm) were scanned and analyzed for immunofluorescence quantification at 647 nm. The nuclei/cytoplasm percentage ratio of NFKB was quantified. Cytotoxicity was determined by cell counting from DAPI staining and expressed as a percentage of cells compared to the control.

Results

Chemical characterization

The particles which were used in this study have been characterized before extensively in two studies (Sieg et al., 2017, Krause et al., 2018). These publications describe the physicochemical parameters of the applied particles in stock dispersions and artificial digestion fluids by a big variety of methods. These results, which form the analytical basis of the following experiments, are summed up in Supplementary Table 1. Both Al-containing nanoparticles showed a size distribution between 10 and 100 nm in stock dispersion. The spherical Al^0 nanoparticles turned out as rather broadly distributed. These particles consisted of metallic particle cores with an oxide layer on the particle surface due to the manufacturing process, which could be shown by TEM and XRD measurements (Krause et al., 2018). To avoid further oxidation, the particles were stored, weighted and diluted under an Argon atmosphere immediate prior to use. Al_2O_3 nanoparticles formed loose agglomerates consisting of elongated single particles with core radii between 4 and 10 nm and lengths between 20 and 40 nm. Both species were rather stable in artificial digestion fluids, showed little ion release and agglomeration in gastric fluid as well as reassembled in intestinal fluid. In addition, $AlCl_3$ formed nanoscaled *de novo* particles in the intestinal fluid (Sieg et al., 2017). A thorough characterization of the nanoparticles in biological systems was still missing but is also required to allow a meaningful interpretation of the results from cellular *in vitro* assays. Therefore, Figure 1 shows results of the characterization of the particles in cell culture medium.

The size distributions of the different nanoparticles and the ion release from these Al species in cell culture medium were investigated. Figure 1A shows nanoscaled particle core size distributions for all applied Al species, derived by SAXS measurements. Distributions were species specific and quite stable over a time period of 48 h. Figure 1B shows ion release of the 3 used Al-species in cell culture medium for 2 different concentrations (4 and 100 µg Al/ml) over a time period of 48 h. Metallic Al nanoparticles showed a significantly higher ion release than Al_2O_3 nanoparticles in both cases. At the low concentration, around 15 % of the totally loaded Al from metallic nanoparticles was released as free ions, while ion release from Al_2O_3 nanoparticles was not detectable over the medium background, which was determined as 0.19 µg/mL in cell culture medium (4.75 % of applied 4 µg/mL, 0.19 % of applied 100 µg/mL). At the higher concentration, the relative ion release by metallic nanoparticles was

much lower (around 1 %), which was still significantly above the released fraction from the Al_2O_3 nanoparticles and the medium background. The ionic Al species showed an almost steady amount of $15 - 25$ % free ions in cell culture medium. The remaining proportion could exist as aggregates, *de novo* emerged particles, polymers and protein complexes. The determination of the protein corona composition surrounding the nanoparticles in serum-containing cell culture medium could also influence interactions between nanoparticles and cells. Figure 1C shows the protein composition of the coronae surrounding both nanoparticle species, separated by 2D-PAGE and analyzed by tryptic digestion and MALDI-TOF-MS. The corona of metallic nanoparticles appeared less complex and contained predominantly enriched β-Actin while the other serum proteins got depleted and were barely detectable in the protein analysis. The corona of Al_2O_3 nanoparticles displayed a more complex composition. The appearance of metal ion interacting proteins (FETA, TRFE, abbreviations defined in the table) and lipid interacting proteins (APOA1) was notable. $AlCl_3$ led to an enriched agglomeration of all detected proteins compared to the basic composition in the serum-containing cell culture medium.
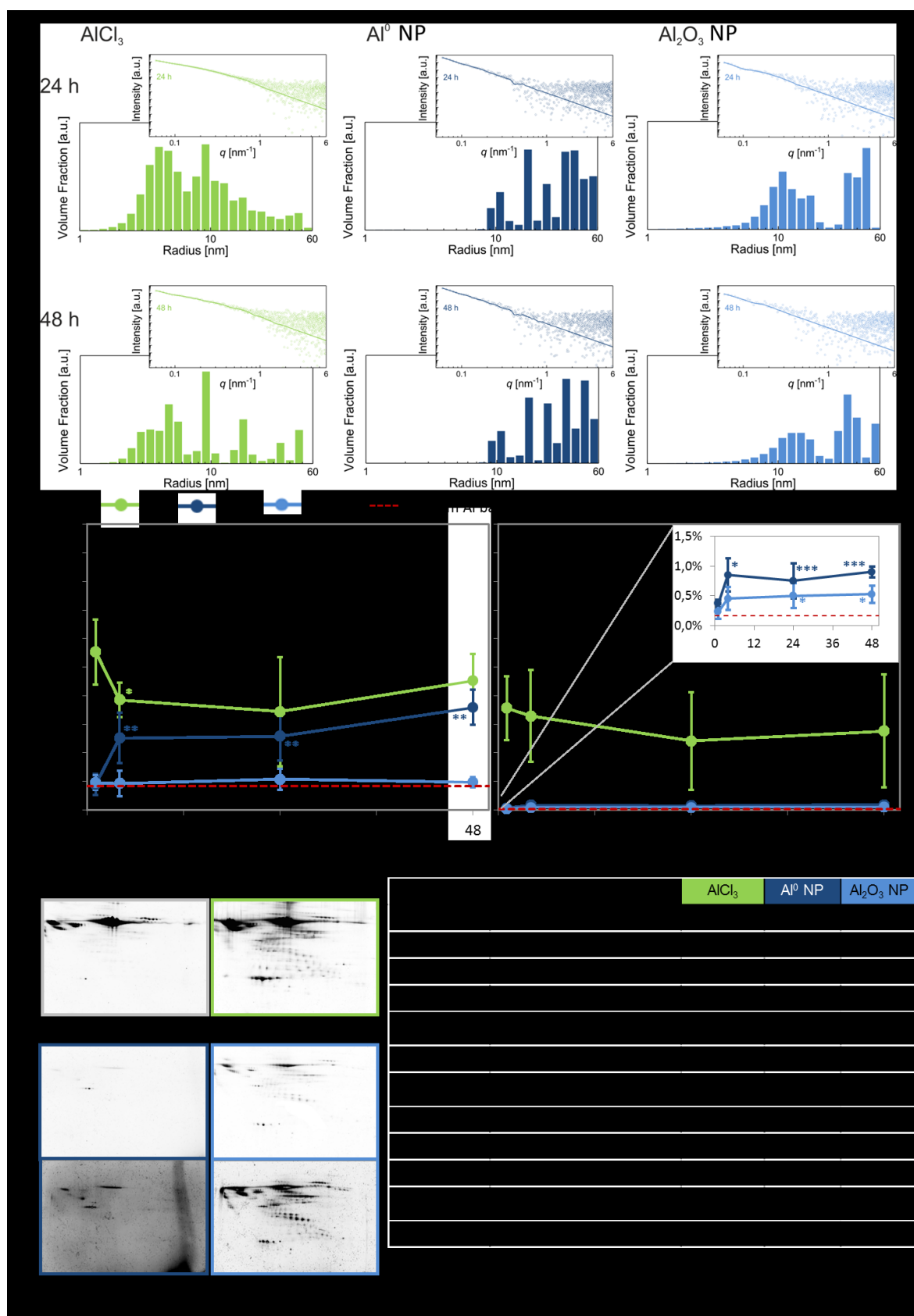
Figure 1: Characterization of nanoparticles. (A) Particle core size as determined by SAXS in cell culture medium (DMEM) after 24 h and 48 h incubation time. (B) Ion release of Al-containing nanoparticles and controls. Quantification of ionic Al was performed via ultracentrifugation, microwave digestion and AAS after incubation of testing substances in serum-containing cell culture medium (CCM) over a time period of 48 h. Relative ionic fraction compared to initial concentration (4

and 100 µg Al/mL), mean values of at least 6 replicates from 3 independent experiments, each with standard deviation, significance determined via Student's t-test indicated by asterisks. Inset shows the lower percentage area. (C) Protein corona analysis. Left: 2D-gel-electrophoresis of corona proteins, isolated by UC after incubation of nanoparticles and controls for 24 h in serum-containing CCM. Gels stained by ruthenium staining and pictures taken by Versadoc gel imager without and with amplification. Right: semi-quantitative evaluation of corona protein enrichment. Protein identities were determined by tryptic digestion and matrix-assisted laser desorption ionization-mass spectrometry (MALDI-TOF-MS).

Cellular uptake and transport

Cellular uptake and transport of the different Al species were investigated in transwell experiments with three different coculture models: the Caco-2 monoculture, a mucus-producing model and an M-cell model (Figure 2A). Incubation of 24 h with Al species was followed by element analysis. The amount of Al detected in the basolateral compartment was defined as transported, while the amount that remained in the washed membrane fraction was defined as taken up by the cells. The apical fraction (apical medium and wash solution) were used for recovery measurements (not shown). Figure 2B and C show no significant transport of Al above the medium Al-background irrespective of the Al species and cell model. However, differences between the Al species were noticed in the uptake. Both Al-containing nanoparticles were taken up into the cells at fractions below 4 % of 50 µg applied Al with minor differences among the cellular models. This was a significantly higher uptake of particulate Al species, as compared to the ionic species which was not taken up to a remarkable degree. This implicates that Al is predominantly taken up as particles, whereas the uptake of dissolved Al ions was avoided through cellular mechanisms. Aluminum recovery, as a sum of all generated fractions, added up to around 50 µg (corresponding to 100 %) with measurement-related standard deviations (Supplementary Figure 1) while the control samples corresponded to the determined Al background of 0.12 – 0.17 µg as a sum of all fractions. Since there were no substantial differences among the cell models, differentiated Caco-2 monocultures were used for the subsequent experiments.

To confirm the uptake of Al and Al_2O_3 nanoparticles and to precisely localize them within the Caco-2 cells, TEM experiments were carried out. Slices cut at mid-height of cells incubated with the nanoparticles or with the ionic control were inspected (Fig 2D). Control and treated Caco-2-cells were lipid droplets rich as expected. Intracytoplasmic nanoparticle uptake was observed for both particle species. Nanoparticles were identified in many clusters, delimitated

by a membrane which is typical for late endosomes as expected from an endocytose pathway. Relatively large amounts of Al^0 and Al_2O_3 nanoparticles were observed inside the cells, consistent with the results from the element analysis. Both particulate forms showed a similar behavior with a compartmentalization of the nanoparticles into late endosomes. In the case of Al nanoparticles, however, only large clusters were observed, whereas as Al_2O_3 nanoparticles were found both as large agglomerates and as isolated particles. In addition, the Al_2O_3 particles are possibly slightly released and/ or deteriorated within the endosomes. In contrast, no particle uptake was observed for the control samples, endosomes without dark content were infrequently observed. Using TOF-SIMS (Figure 2E), the 3D depth profile of the cells, depicted as translucent green with Al^0 nanoparticles in dark blue color and Al_2O_3 in light blue, showing clearly the intracellular localization of Al^0 nanoparticle aggregates. The cells, which were exposed to Al_2O_3 nanoparticles are showing the cell monolayer in translucent green and with Al_2O_3 nanoparticles in blue color, showing clearly the intracellular localization of Al_2O_3 nanoparticle aggregates. IBM (Figure 2F) displays the element distributions of Al, phosphorous and sulfur among differentiated Caco-2 cells after incubation with Al species. In untreated control cells as well as in Caco-2 cells incubated with Al_2O_3 nanoparticles, only a background level of Al was visible, which was lower than the methodical limit of detection and therefore not quantifiable. In contrast, cells incubated with Al^0 nanoparticles showed a clear association between the cells and Al.
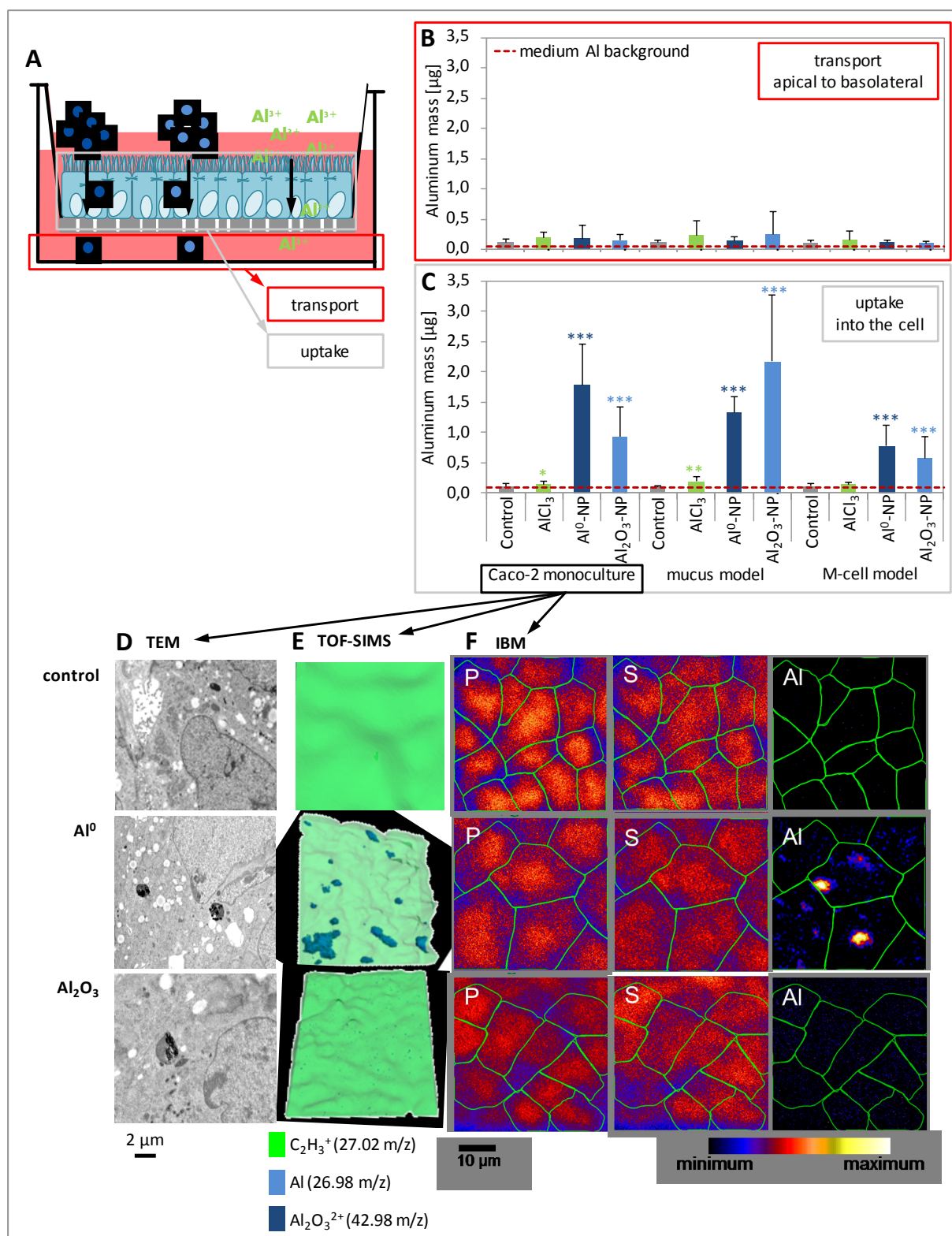
Figure 2: Analysis of transport and uptake of aluminum species in *in vitro* models. (A) Schematic overview over the used *in vitro* model. Quantification of transport into the basolateral compartment (B) and cellular uptake (C) of Al-containing nanoparticles and controls in transwell experiments with differentiated Caco-2 cells and cocultures after incubation with testing substances (100 µg Al/mL) for 24 h. Al-amount determined by microwave digestion of basolateral compartment (transport) and washed membrane fraction (uptake) followed up by AAS measurements. Each experiment was repeated at least 3 times with 3 replicates of each sample with standard deviation, significance

determined via student's t-test indicated by asterisks. (D, E and F) Distribution and cellular localization of aluminum species in Caco-2 monolayer analyzed by (D) Transmission Electron Microscopy (TEM), (E) Time-of-Flight secondary ion mass spectrometry (TOF-SIMS) and (F) µPIXE images. (D) TEM pictures of differentiated Caco-2-cells incubated with 100 µg/mL Al particles or 188.7 µg/mL Al_2O_3 particles after 24 h of treatment and compared to control Caco-2-cells. Cells were transversally sectioned at 90 nm thickness after resin-embedding (Epon). (E) TOF-SIMS reconstructed depth profiles (positive mode), showing the aluminum in blue color at m/e 26.98 u and organic matter from differentiated Caco-2 cells at 27.02 u ($C_2H_3^+$) in green color. The upper spectrum shows a depth profile of differentiated Caco-2 cells, treated for 24 h with controls, the middle spectrum with 100µg Al/ml Al^0 nanoparticles (ca. 20nm) and the lower spectrum with 100 µg Al/mL of Al_2O_3 nanoparticles. (F) IBM µPIXE element maps reveal an area of 50 x 50 µm². Black color represents the lowest, while white shows the highest local element concentration. The mass density of Al is shown. Furthermore, cellular matrix elements phosphorus and sulfur are displayed. Caco-2 cells exposed to 100 µg/mL Al^0 and Caco-2 exposed to 100 µg/mL Al_2O_3 (corresponding to 52.93 µg Al/mL) are displayed. The green lines exhibit the borders of the cells, determined by the phosphorus and sulfur signal.

Cellular and molecular effects

Initially, cell viability testings such as CTB, MTT, apoptosis- / necrosis- and cellular impedance measurements were done to determine applicable experimental conditions (Figure 3). None of the Al-species showed increased cytotoxicity on differentiated Caco-2 cells over 48 h of treatment. Only a weak toxic effect was observed with a high concentration of 200 µg Al/mL of ionic $AlCl_3$. Similarly, no induction of apoptosis or necrosis, as well as no effects on cellular impedance was observed.
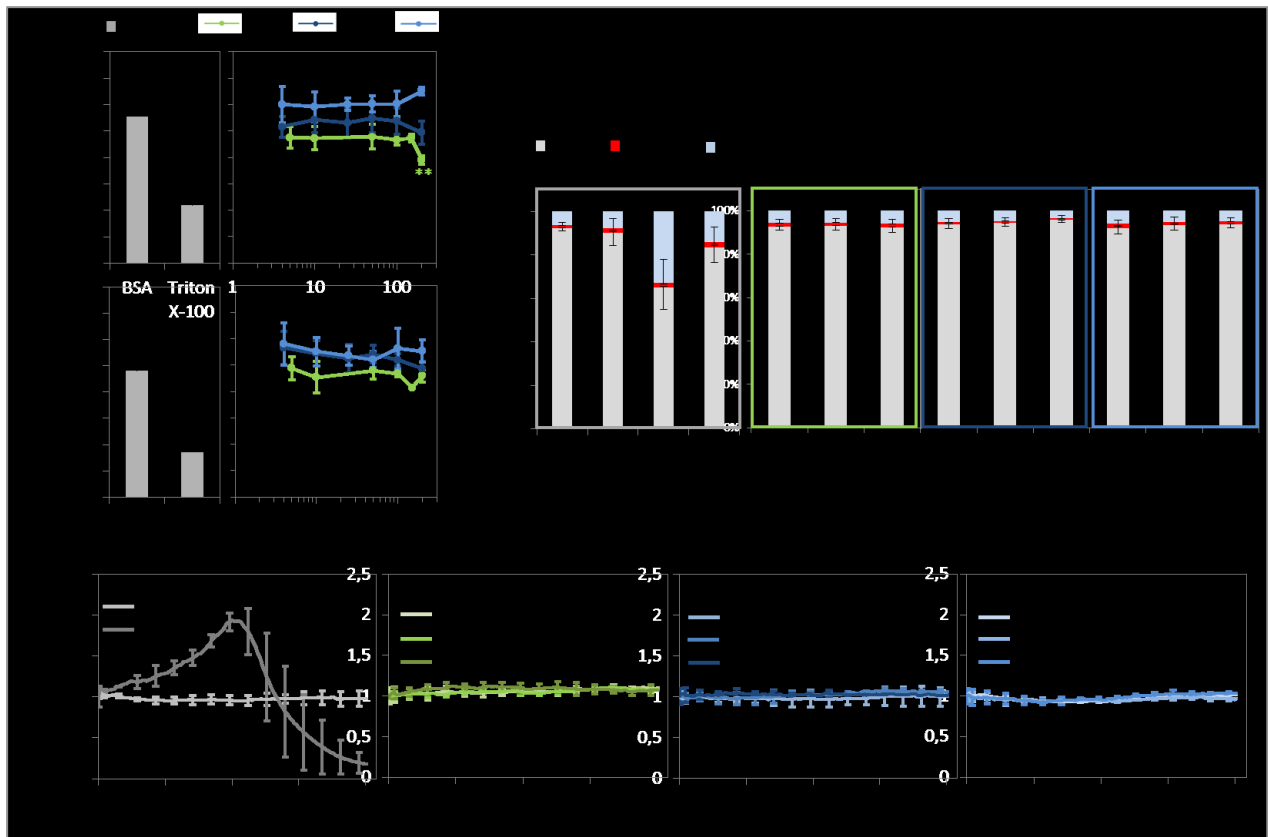
Figure 3: Measurements of toxicological endpoints after 24 h incubation of differentiated Caco-2 cells after incubation with Al-species. (A and B) Relative viability after 48 h incubation with Al-species, shown by CTB (A) and MTT (B). 0.01 % Triton X-100 was used as positive control. (C) Apoptosis- / necrosis measurements determined by flow cytometry with Annexin-V / 7-AAD staining. As positive controls, 2 µM staurosporine and 50 mM tert-butyl hydroxyperoxide were used. (D) Measurements of cellular impedance by xCELLigence technology after incubation with Al-species over a time period of 48 h. Relative cell indices normalized on initial cell index and medium control. Mean values calculated out of at least 3 replicates indicated by standard deviation. ZnO nanoparticles (100 µg Zn/ml, supplied by IoLiTec) were used as positive control. Results normalized on medium control as mean values of at least 3 independent experiments indicated by standard deviation. Significance determined via student's t-test indicated by asterisks.

After determination of cytotoxicity, regulatory effects of Al-containing nanoparticles and controls were investigated by an untargeted transcriptome screening analysis via microarrays under non-toxic conditions. Figure 4A shows Venn-diagrams of the deregulated genes of differentiated Caco-2 cells by each Al species. While there was only a moderate number of deregulated sequences for the particulate Al species (298 for Al^0, 401 for Al_2O_3), there were much more deregulated sequences resulting from treatment with ionic Al (1336). Many of those deregulated sequences were not annotated because they belong to unknown sequence segments. Some of them belong to regulatory elements, miRNAs, snRNPs, spliceosomal subunits or pseudogenes and only a smaller amount stands for protein coding sequences. Our

results highlight that effects of Al-containing nanoparticles are rather low compared to the considerable effects caused by ionic species. These effects were obtained by *in silico and in vitro* testing methods. The gene regulation of 8 significantly regulated genes of different treatment groups was verified via qPCR, whichis shown in Figure 4B and Supplementary Figure 2.

The results of the *in silico* evaluation of the transcriptome analysis is shown in Figure 4C and Table 1. IPA analysis (Table 1) gives indications for involved signaling pathways. Predictions include, besides others, canonical pathways and toxicological mechanisms. With respect to the underlying array data, the predictions vary in their significance. Especially because the transcriptome analysis showed rather moderate fold changes and hit numbers, some of the predictions do not reach the significance level and therefore should be interpreted with care. Basically, there are more meaningful predictions for the $AlCl_3$ treatment group, where the highest number of deregulated genes was found as well. IPA was only able to predict involvement of the relevant pathways, but not the direction of the regulation, i.e. up- or downregulation of the involved pathways. The data from treatment with ionic $AlCl_3$ pointed towards the involvement of xenobiotic response pathways such as CAR and PXR/RXR, or mechanisms that indicate stress reactions like glutathione (GSH) level changes or mitochondrial dysfunction. The predictions for elementary Al^0 nanoparticles focused as well on glutathione depletion and CAR/RXR activation. In this group, the significance levels were much lower and the predictions more limited because of the lower effects given from the microarrays. The predictions caused by Al_2O_3 nanoparticles concentrated on xenobiotic metabolism and the cytochrome P450 panel, which was predicted for $AlCl_3$ as well with a higher significance. Effects on xenobiotic metabolism were found in all treatment groups, from which the predictions in the $AlCl_3$ group showed the strongest significance and also the involvement of the PXR/RXR signaling pathway.

The program "geneontology" (Figure 4C) indicated grouping of the regulated genes in relation to their cellular localization, protein function and involvement into biological processes. The bars show the fraction of the identified genes of each group which are related to the individual process, function or cellular localization. This provides hints about cellular processes which are influenced by the respective treatment. Although the predictions have to be interpreted with caution, tendencies were observable. Many detected sequences refer to stress response, metal ion interaction or metal binding activities. The relative amounts of each

protein group did not differ much among the different species, which speaks for almost similar mode of actions that are only in a lower extent for particulate species, and therefore less significant, but following the same mechanistic principles. Probably the weak cellular response observed with Al-containing nanoparticles is related to the lower amount of free ions that are released from the particles compared to the ionic controls. Interestingly, protein fractions assigned to the predicted functions and processes caused my Al^0 nanoparticles were even lower than for both other species, what corresponds to the lower effects detected in the microarrays. This does not correspond to the ion release, which is higher than the ion release from Al_2O_3 nanoparticles. The predictions for cellular localization appeared not to prefer any protein class and distributed equally over the different compartments. Here, the weakest predictions are made for Al^0 nanoparticles again. This is also valid for the protein functions. Our results suggest that both particulate species did not induce any particle-specific reaction.
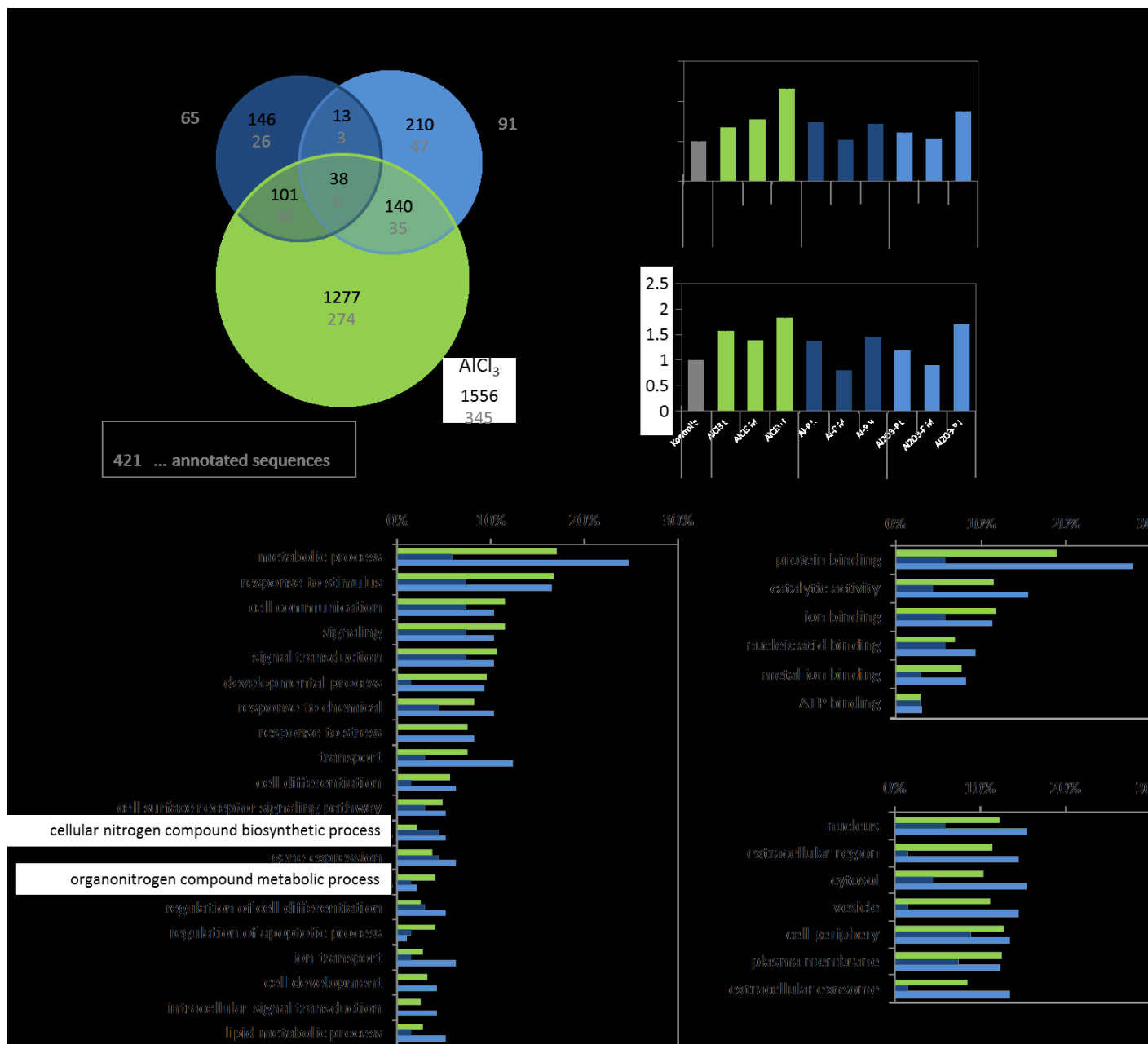
Figure 4: Results of microarray analysis. (A) Venn diagram comparison of deregulated primary hits (black numbers) and annotated sequences (grey numbers) determined by microarray analysis of differentiated Caco-2 cells incubated with Al species (50 µg Al/mL) for 24 h. (B) Quantitative real time RT-PCR for selected genes ABCC3 and COG7. Further genes are depicted in Supplementary Figure 2. (C) Results of *in silico* analysis of the fractions of regulated genes related to a specific cellular localization, protein function and biological processes by "geneontology" software. Significance defined by 3 out of 3 replicates with a fold change > 1.5 up or down and ANOVA p-value < 0.05.

Table 1: Results of predicted influence on canonical pathways and TOX-lists by IPA analysis. Al-species were compared to the medium control, Significance defined by 3 out of 3 replicates for genes with a fold change > 1.5 up or down and ANOVA p-value < 0.05. Pathway predictions with a p-value above 0.05 are not statistically significant and therefore indicated in italics.

		PXR/RXR Activation	*5,50E-02*
		PTEN Signaling	*9,33E-02*
		Epithelial Adherens Junction Signaling	*1,12E-01*
Lactose Degradation III	*5,37E-02*	*Hepatic Cholestasis*	*1,32E-01*
Regulation of Cellular Mechanics by Calpain Protease	*5,89E-02*	*LPS/IL-1 Mediated Inhibition of RXR Function*	*1,66E-01*
Phototransduction Pathway	*6,46E-02*	*Systemic Lupus Erythematosus Signaling*	*1,70E-01*
Pyruvate Fermentation to Lactate	*6,61E-02*	*Xenobiotic Metabolism Signaling*	*2,09E-01*

PXR/RXR Activation	*5,13E-02*		
Hepatic Cholestasis	*1,23E-01*		
LPS/IL-1 Mediated Inhibition of RXR Function	*1,86E-01*	*Cardiac Necrosis/Cell Death*	
Xenobiotic Metabolism Signaling	*2,45E-01*	*TR/RXR Activation*	
Renal Necrosis/Cell Death	*3,47E-01*	*p53 Signaling*	
		Fatty Acid Metabolism	
		LXR/RXR Activation	

To see, if the predicted molecular effects were reflected on the cellular level, we chose several toxicological endpoints like GSH level, ATP level, mitochondrial membrane potential, IL-8 release and NFκB nuclear translocation, shown in Figure 5A-E.
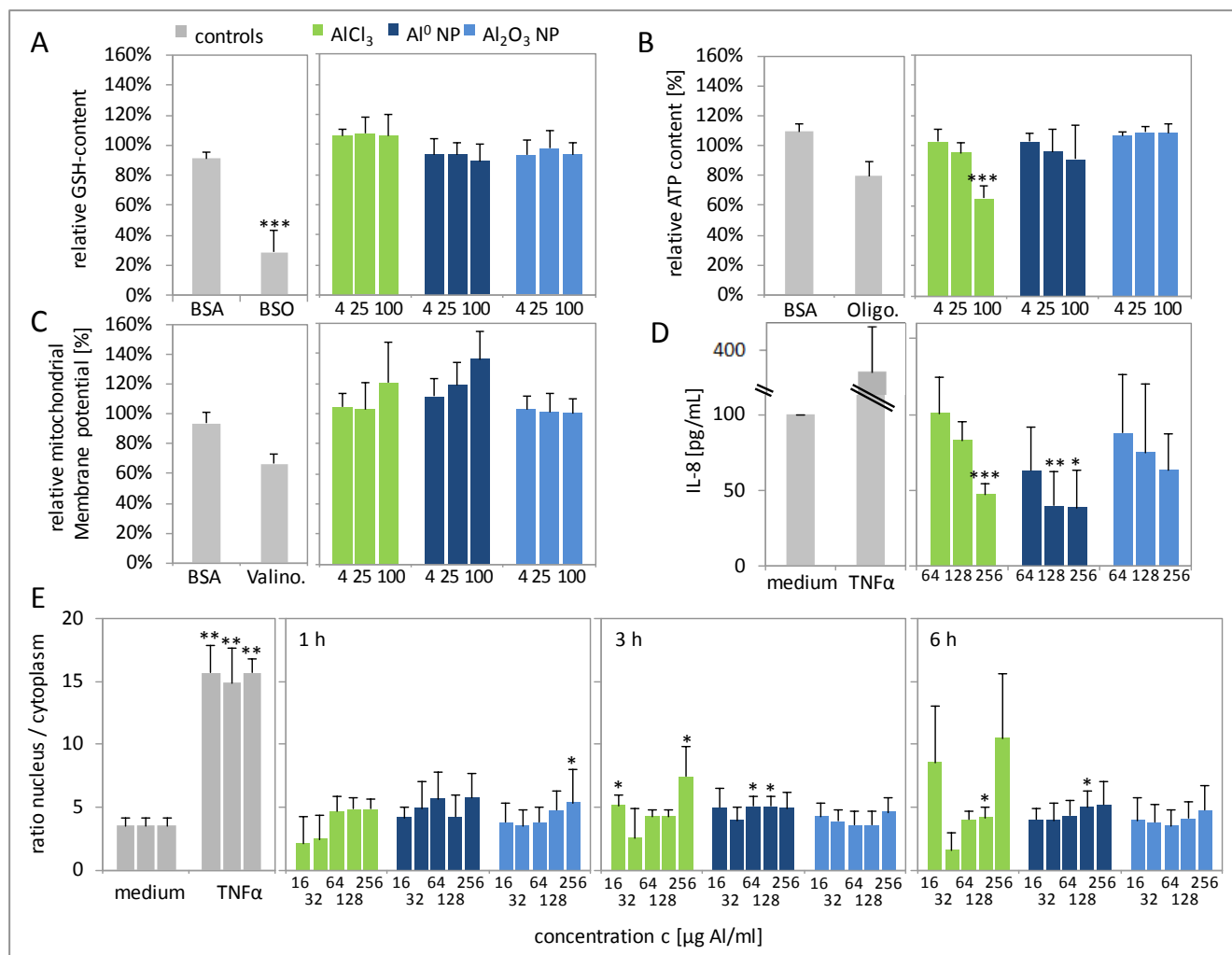
Figure 5: Measurements of toxicological endpoints of differentiated Caco-2 cells after 24 h incubation with Al-species. (A) Determination of relative GSH-levels determined by monochlorobimane assay. (B) Relative cellular ATP-levels determined by Cell Titer Glo-assay. (C) Relative mitochondrial membrane potentials determined by JC1-assay. (D) IL-8 release from differentiated Caco2 cells after 24h nanoparticle exposition. As positive control, 20 ng/mL TNFα was used. Values are presented as the mean percentage ± SD (n = 3). *** indicate significantly higher levels compared to controls corresponding to p < 0,001, student's t-test. (E) Nuclear NFĸB translocation after 1, 3 or 6 hours treatment with different concentrations of Al species. Positive control TNFα 20 ng/mL. Values are presented as the mean percentage ± SD (n = 3). *,**,*** indicate significantly higher levels compared to controls corresponding respectively to p < 0.05, p < 0.01, p < 0.001, Student's t-test. Results normalized on medium control as mean values of at least 3 independent experiments indicated by standard deviation. Significance was determined via student's t-test indicated by asterisks. As positive controls 100 μM BSO (A), 1 μM oligomycin (B), 1 mg/mL valinomycin (C), and TNFα (D and E) were used.

No effects on GSH levels or mitochondrial membrane potential were measured, irrespective of the Al-species. ATP level measurements showed a significant and concentration dependent

decrease of ATP at high concentrations of ionic Al in contrast to the particulate species at the same concentrations. An interaction of Al with this luciferase testing system was already published and a correction factor was taken into account to subtract this interaction as described in the referred article. The levels of IL-8 release were studied by an ELISA assay which showed a non-significant increase compared to the control after 24 h of treatment. Similarly, the transcription factor NFκB, which is translocated into the nucleus of cells as early event of inflammatory stimulation, showed only a slight increase with Al^0 nanoparticles (at 3 h and 6 h) and Al_2O_3 nanoparticles (at 1 h for the highest concentration). The effect of $AlCl_3$ depicted a large variability but without any dose-response-relationship. Those results confirmed the absence of an inflammatory effect of Al and Al_2O_3 nanoparticles and $AlCl_3$.

Discussion

In this work, several analytical and toxicological questions concerning orally taken up Al were addressed. First, the issue of species-dependent ion release from Al-containing nanoparticles in presence of biological media was investigated. In nature, Al is mostly bound in minerals forming oxide species (Yokel and McNamara, 2001). Metallic species are mainly produced by humans and are so transferred into the biological cycles. In addition, industrial processes acidify the environment and increase therewith the availability of dissolved, ionic Al (Exley, 2003, Martin, 1994). Ionic Al also derives from food packaging and kitchen ware (Liukkonen-Lilja and Piepponen, 1992, Verissimo et al., 2006) or gets dissolved along the gastrointestinal tract (Schönholzer et al., 1997, Froment et al., 1989a). Therefore, to investigate effects of Al, it is necessary to have detailed knowledge about the chemical state of the Al that is observed. The physico-chemical parameters of the 3 Al species used in this study have been measured with complementary methods.

The volume-weighted distributions of the core gyration radii were determined by SAXS measurements. The advantage of SAXS is that a measurement direct in complex matrices like cell culture medium is possible. Since the aluminum nanoparticles scatter much stronger than the surrounding cell culture medium, SAXS is an appropriate method for the determination of the core radii. For the Al_2O_3 nanoparticles a bimodal size distribution consisting of small particles and aggregates is depicted (Figure 1A). After an incubation time of 24 h in cell culture medium, the primary particles showed a radius of 13.6 ± 0.6 nm, whereas the aggregates exhibited radii > 30 nm. A longer incubation (48 h) resulted in a slight increase in the small particles' radii to 15.7 ± 0.8 nm. For the Al^0 nanoparticles a distinct differentiation of different size populations was not possible. Instead, the size distribution after 24 h showed particles with radii > 10 nm, which remained the same for an incubation time of 48 h. As already discussed in the preliminary study of the stock solutions (Sieg et al., 2017) the incubation of ionic Al in form of $AlCl_3$ in cell culture medium resulted in a nanoparticle formation. During the incubation time of 24 h and 48 h the formed particles showed radii in the range of $2 - 60$ nm with a broad size distribution. All in all, the particles size distribution for all three Al species did not change significantly upon incubation in cell culture medium for 24 h and 48 h.

We showed that metallic Al^0 particles are more susceptible to ion release in biological media than Al_2O_3 nanoparticles (Figure 1). This effect was concentration-dependent as the fraction of released Al-ions was much higher at low Al-concentrations (15 % at 4 µg Al/mL and only 1 % at 100 µg Al/mL). This process can be two-directional, meaning that free ions can also form *de novo* particles or aggregates. This effect was described before for other elements (Lichtenstein et al., 2015, Juling et al., 2016, Hansen and Thünemann, 2015) and also for Al species in artificial digestion fluids (Sieg et al., 2017). $AlCl_3$ was present in the form of free ions only in a proportion of around 20 – 30 % irrespective of the loaded concentration. The present composition of Al species has an influence on bioavailability and cellular uptake of Al. Generally, soluble Al shows more systemic bioavailability than Al from solid species (Van Oostdam et al., 1990, Yokel et al., 2005, Krewski et al., 2007). Most Al is resorbed by the proximal section of the human duodenum (Froment et al., 1989b). In our experiment, we investigated the species-specific uptake and passage of Al into the intestinal barrier. Therefore, we used three different cell culture models (Caco-2 monoculture, mucus model, M-cell model). Al uptake and transport were measured by element analysis. While there was no transport through the membrane detectable for all species (Figure 2B), we could observe differences in cellular uptake (Figure 2C). Among all three culture models, particulate species were measurable taken up into the (washed) membrane fraction. There was no measurable difference among the models and also not between both particle species, but there were strong differences to ionic Al species, which were taken up rarely into the cell fraction. While no transport through the in vitro intestinal models for the 3 Al forms was detected, results on cellular uptake highlighted that both NP forms were taken up by cells but rarely $AlCl_3$. This particle-specific cellular uptake was already known for other nanoparticles and described as "trojan-horse-effect" (Hsiao et al., 2015, Semisch et al., 2014). Particles were taken up incidentally while the cells have mechanisms to keep metal ions actively out. TEM experiments are consistent with elemental analysis, since they clearly show the uptake of the particles. This result is no contradiction to the previously preferred ionic intestinal bioavailability, because an uptake into epithelial cells does not necessarily mean systemic transport. Intestinal epithelial cells, with or without particles, have a lifetime of around 72 h and are excreted by the gut. So only transported Al is systemic bioavailable.

The 3D TOF-SIMS depth profiles of the cells showed clearly the intracellular localization of Al^0 nanoparticle aggregates in cells exposed to Al^0 nanoparticles. The cells, which were exposed to Al_2O_3 nanoparticles showed as well clearly the intracellular localization of Al_2O_3

nanoparticle aggregates. No aluminum could be detected within unexposed Caco-2 control cells. In Caco-2 cells, which were exposed to ionic aluminum ($AlCl_3$) only very few very small aluminum clusters could be detected within the whole culture, and these clusters seemed to localize in specific areas. However, TEM showed relatively similar patterns for Al and Al_2O_3 nanoparticle clustering. In case of µPIXE analysis, the Al detection limit was higher than the natural Al background of control cells. Caco-2 cells exposed to Al_2O_3 didn't reveal an uptake larger than the detection limit. The aluminum pattern for cells exposed to Al^0 nanoparticles exhibited a clear uptake of aluminum. This is in good consistence to TEM and TOF-SIMS results.

The absence of transport across the transwell membrane could be due to experimental issues. Transwell systems show elevated barrier function and so limit paracellular crossing compared to the *in vivo* situation (Artursson and Karlsson, 1991). In addition, persorption due to intestinal regeneration processes are not mimicked by this system (Volkheimer, 1974). Nevertheless, transwell experiments often show a suitable control for intestinal uptake and transport of some nanoparticle species (Gullberg et al., 2000, des Rieux et al., 2005, Walczak et al., 2015, Lichtenstein et al., 2016, Lin et al., 2012, Bouwmeester et al., 2011).

Another influencing parameter on particle stability, agglomeration and biological interaction is the composition of the specific protein corona (Figure 1C). Our results show differences of protein identities between both particle species. Metallic Al nanoparticles showed a slightly complex protein distribution, where mainly β-actin was enriched. Al_2O_3 nanoparticles showed a more complex variety of corona proteins. It was already shown, that serum proteins can have influence on the toxicity of metal ions (Haase et al., 2015). In this context, proteins like serum albumin (Uniprot abbreviation: ALBU), transferrin (TRFE), apolipoprotein A1 (APOA1) and α-glycoprotein (FETUA) and β-actin (ACTB) were shown to interact with metal homeostasis and endocytosis activity (Waheed et al., 2008, El Hage Chahine et al., 2012, Yang et al., 2013, Lewis and Andre, 1981, Conner and Schmid, 2003), that have been detected in this study, too.

Recently, the toxicological effects of Al have been largely discussed. Dialyzed patients suffering encephalopathy and osteomalacia were correlated with elevated Al levels in blood and organs (Alfrey et al., 1976, Vick and Johnson, 1985). The cation chelator deferoxamin which complexes Al ions was found to alleviate the symptoms (Felsenfeld et al., 1989).

Current research focusses on a link with breast cancer (Darbre, 2009) and Alzheimer's disease (Walton, 2014, Percy et al., 2011), which although is disputed (Lidsky, 2014). In this study, a broad concentration range from 4 – 200 μg Al/mL was chosen. With an estimated Al consumption of 0.2 – 2.3 mg / kg bw/week and a TWI of 1 mg / kg bw/week (EFSA, 2011), the lower part of the scale (4 – 10 μg Al/mL) corresponds to a realistic oral Al exposure. The upper end of the scale corresponds to the highest possible exposure derived from the maximal Al contents found in food products such as mollusks, paprika, cocoa powder and blackboard salt with more than 100 mg/kg food mass (Stahl et al., 2011, Arnich et al., 2012, Millour et al., 2011). Above 200 μg Al/mL, toxic effects of Al on Caco-2 cells are described (Zhou and Yokel, 2005). 100 μg Al/mL were found out to be non-toxic on Caco-2 cells with multiple assays (Figure 3) and so could be used for cellular uptake experiments. To avoid unspecific stress reactions in the very sensitive transcriptome analysis, a lower concentration of 50 μg Al/mL was used for the microarrays. The microarray study showed rather moderate deregulation of genes, what nevertheless allowed predicting the involvement of xenobiotic metabolism, oxidative stress response and metal ion homeostasis, mainly in the treatment group with ionic $AlCl_3$. *In vitro*, these effects caused by Al^{3+} ions were described on cellular level as oxidative damage (Zatta et al., 2002), indicated by membrane lipid peroxidation (Gutteridge et al., 1985, Fraga et al., 1990). Comparable effects were also described for particulate Al_2O_3 (Zhang et al., 2011). This leads further to a destabilization of the cell membrane (Amador et al., 1999). Another described key effect of Al is the competition with essential metal ions such as iron (Mujika et al., 2011), magnesium (Martin, 1994) and calcium (Mundy et al., 1997), due to their chemical resemblance (Zatta et al., 2002). Al has a strong affinity to essential cellular compounds such as phosphate and influences enzymatic functions of the antioxidative system (Zatta et al., 2002). Al has a strong affinity to essential cellular compounds such as phosphate and influences enyzmatic functions of the antioxidative system (Zatta et al., 2002, Kong et al., 1992, Hasanoglu et al., 1994, Atienzar et al., 1998). Our *in silico* methods predicted that metal ion homeostasis, xenobiotic metabolism and oxidative stress response could be affected (Figure 4, Table 1). Nevertheless, our *in vitro* results showed that at least for the differentiated Caco-2 cell model, most relevant endpoints were not affected. A significant change in cellular ATP levels that can result from oxidative stress was only reported with $AlCl_3$. Even if the cellular uptake of Al-containing nanoparticles was higher, no specific nanoparticle effect which was detected. We conclude, that effects are mainly caused by the released Al ions, what is underlined by the *in silico* microarray predictions.

Conclusion

Cellular uptake, bioavailability, metabolism and toxicological effects of Aluminum are species-specific and controversially discussed. We have shown for the first time that intestinal cellular uptake of Al occurs preferably in the particle form, while toxicological effects appear to be ion-related. Regarding this, in biological systems, such as the gastrointestinal tract, there occurs a transition of particulate to ionic Al species as well as reverse. The proteomic composition of the biological interface is also species-specific, as well as the quantity of released Al ions from different nanoparticles. Toxicological effects of Al target cellular metal ion interaction, oxidative damage and xenobiotic metabolism. Acute toxic effects were mainly found with high $AlCl_3$ concentrations in intestinal cells. Systemic exposure is still under debate as no *in vitro* crossing of the intestinal barrier was detected using 3 different human intestinal cell models. With contemplation to these results in question of uptake, cellular effects and toxicological potential, the resultant impact of Al on human health is not completely foreseeable. Small acute effects imply investigations of long term effects with regard to the respective Al species, which can vary in their quality and quantity of effects. Therefore, Al will stay in the focus of research and risk assessment in the following years.

Supplementary data

Supplementary Table 1: Particle characterization parameters. The particle characterization of the applied nanoparticles was already published (Sieg et al., 2017, Krause et al., 2018) and is summed up in this table.

Parameter	Al⁰ NP	Al₂O₃ NP	Method	Published source
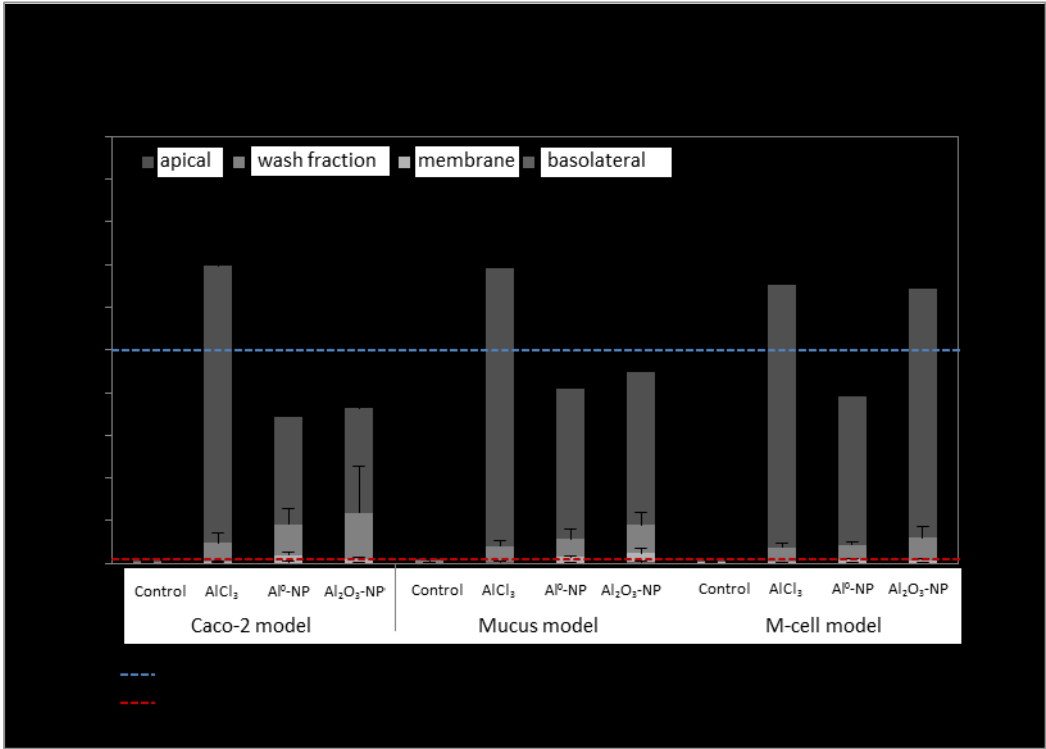
Supplementary Figure 1: Aluminum recovery from Al-containing nanoparticles and controls in transwell uptake experiments with differentiated Caco-2 cells and cocultures after incubation with testing substances (100 µg Al/mL) for 24 h. The Al amount was determined by microwave digestion of all compartments (apical, wash fraction, membrane and basolateral compartment) followed by AAS

measurements. Medium background is depicted by the red line, total applied Al (50 µg) is depicted by the blue line. Each experiment was repeated at least 3 times with 3 replicates of each sample, shown with standard deviation. The detected total Al recovery corresponds approximately to the applied Al mass of 50 µg with measurement-related standard deviations. The Al mass detected in the control sample corresponds to the Al background level.
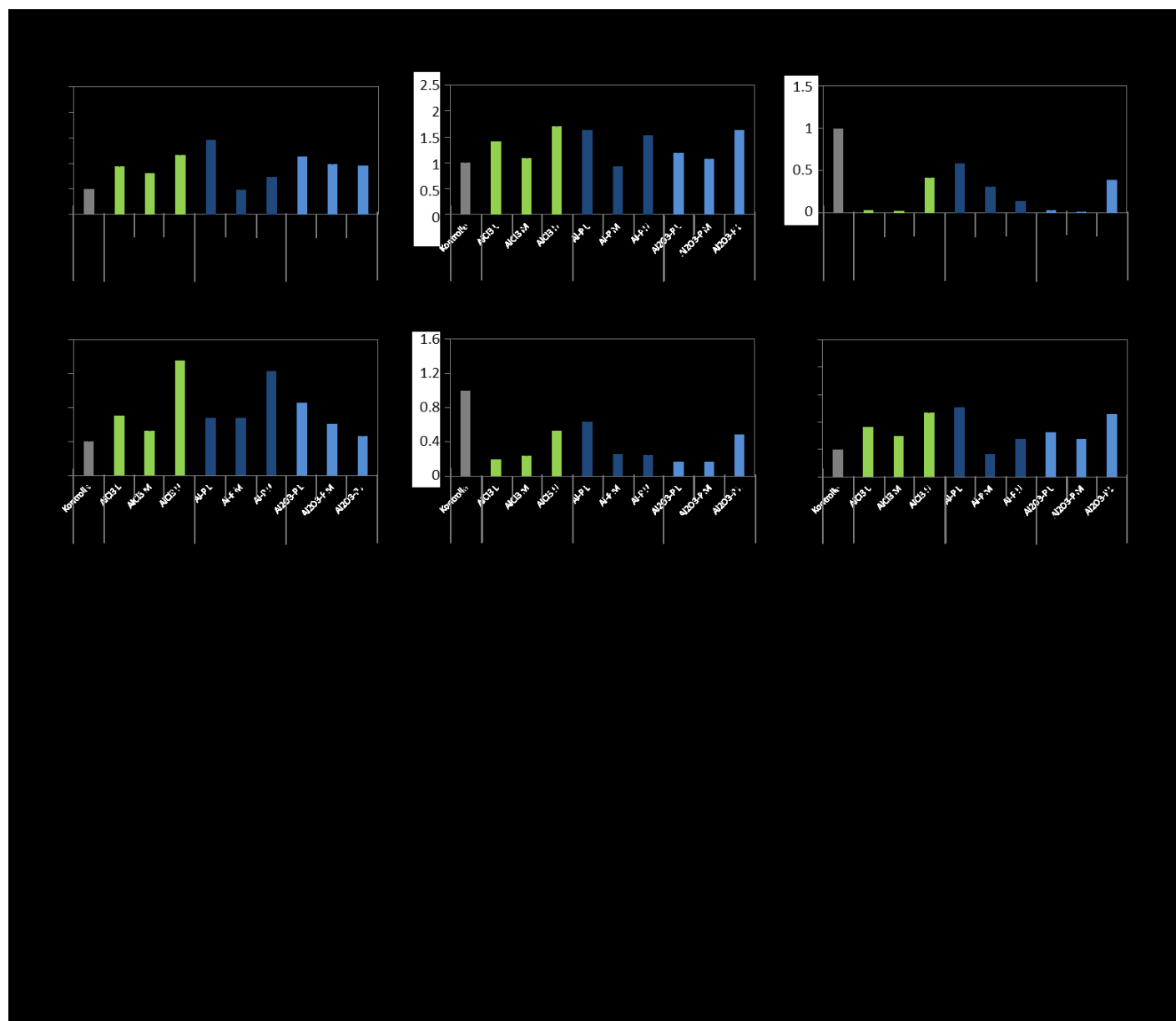
Supplementary Figure 2: Verification of the genes TAS2R50, TRPC3, YWHAEP1, SPARC, ATP6V0CP3 and MAGI1 via qPCR. Representative highly up- or downregulated genes of different sample groups were selected for the verification. The table shows a comparison of the fold changes determined from the microarray analysis and the fold changes calculated by qPCR.

List of abbreviations

2D-SDS-PAGE	two-dimensional gel electrophoresis
7AAD	7-Aminoactinomycin D
μPIXE	Micro-particle induced x-ray emission
AAS	atomic absorption spectroscopy
Al	Aluminum
AxV	Annexin V
BSO	buthionine sulfoximine
CCM	cell culture medium
CTB	Cell Titer Blue assay
DAPI	4',6-diamidino-2-phenylindole
DMEM	Dulbecco's Modified Eagle Medium
ELISA	Enzyme-Linked Immunosorbent Assay
FCS	fetal calf serum
FITC	fluorescein
GSH	glutathione
HCS	High Content Screening
HRP	Horseradish peroxidase
IBM	ion beam microscopy
IPA	Ingenuity Pathway Analysis
MALDI-TOF	matrix assisted laser desorption ionization – time of flight
MCB	monochlorobimane
MS	mass spectrometry
MTT	3-(4,5-Dimethylthiazol-2-yl)-2,5-diphenyltetrazolium bromide
NEAA	non-essential amino acids
NP	nanoparticles
OM	oligomycin
qPCR	quantitative real-time polymerase chain reaction
SAXS	Small-angle X-ray scattering
SD	standard deviation
tBOOH	tert-butyl-hydroxyperoxide
TEER	transepithelial resistance
TEM	transmission electron microscopy
TNF-α	Tumor necrosis Factor alpha
TMB	3,3',5,5'-tetramethylbenzidine
ToF-SIMS	time-of-flight secondary ion mass spectrometry
UC	ultra-centrifugation

<u>Declarations</u>

<u>Availability of data and material</u>

The datasets generated and analysed during the current study are available from the corresponding author on reasonable request.

<u>Competing interests</u>

The authors declare that there is no competing of interest.

<u>Authors' contributions</u>

PL, ALa, VF, LB, DL, IE-L and ALu designed, supervised the project. HS, CB, BMK, HD, CK, B-CK, TM, PJ, KH, SC, HJ and JT performed the experiments, generated the data and discussed the findings. HS, CK, PJ, TM, KH, LB, AB and FG prepared the manuscript and AFT, ALu, JM, ALa, VF, DL and IE-L further improved the manuscript. All authors read and revised the manuscript and agreed on publication.

<u>Ethics approval and consent to participate</u>

Not applicable

<u>Consent for publication</u>

Not applicable

References

ALFREY, A. C., LEGENDRE, G. R. & KAEHYNE, W. D. 1976. The dialysis encephalopathy syndrome. Possible aluminium intoxication. *New Engl J Med,* 294.

AMADOR, F. C., SANTOS, M. S. & OLIVEIRA, C. R. 1999. Lipid peroxidation facilitates aluminum accumulation in rat brain synaptosomes. *J Toxicol Environ Health A,* 58**,** 427-35.

ARNICH, N., SIROT, V., RIVIERE, G., JEAN, J., NOEL, L., GUERIN, T. & LEBLANC, J. C. 2012. Dietary exposure to trace elements and health risk assessment in the 2nd French Total Diet Study. *Food Chem Toxicol,* 50**,** 2432-49.

ARTURSSON, P. & KARLSSON, J. 1991. Correlation between oral drug absorption in humans and apparent drug permeability coefficients in human intestinal epithelial (Caco-2) cells. *Biochem Biophys Res Commun,* 175**,** 880-5.

ATIENZAR, F., DESOR, D., BURNEL, D., KELLER, J. M., LEHR, P. & VASSEUR, P. 1998. Effect of aluminum on superoxide dismutase activity in the adult rat brain. *Biol Trace Elem Res,* 65**,** 19-30.

BOOTH, A., STORSETH, T., ALTIN, D., FORNARA, A., AHNIYAZ, A., JUNGNICKEL, H., LAUX, P., LUCH, A. & SORENSEN, L. 2015. Freshwater dispersion stability of PAA-stabilised cerium oxide nanoparticles and toxicity towards Pseudokirchneriella subcapitata. *Sci Total Environ,* 505**,** 596-605.

BOUWMEESTER, H., POORTMAN, J., PETERS, R. J., WIJMA, E., KRAMER, E., MAKAMA, S., PUSPITANINGANINDITA, K., MARVIN, H. J., PEIJNENBURG, A. A. & HENDRIKSEN, P. J. 2011. Characterization of translocation of silver nanoparticles and effects on whole-genome gene expression using an in vitro intestinal epithelium coculture model. *ACS Nano,* 5**,** 4091-103.

BUHRKE, T., SCHULTRICH, K., BRAEUNING, A. & LAMPEN, A. 2017. Comparative analysis of transcriptomic responses to repeated-dose exposure to 2-MCPD and 3-MCPD in rat kidney, liver and testis. *Food Chem Toxicol,* 106**,** 36-46.

CASTIAUX, V., LALOUX, L., SCHNEIDER, Y. J. & MAHILLON, J. 2016. Screening of Cytotoxic B. cereus on Differentiated Caco-2 Cells and in Co-Culture with Mucus-Secreting (HT29-MTX) Cells. *Toxins (Basel),* 8.

CONNER, S. D. & SCHMID, S. L. 2003. Regulated portals of entry into the cell. *Nature,* 422**,** 37-44.

DARBRE, P. D. 2009. Underarm antiperspirants/deodorants and breast cancer. *Breast Cancer Res,* 11 Suppl 3**,** S5.

DES RIEUX, A., FIEVEZ, V., THEATE, I., MAST, J., PREAT, V. & SCHNEIDER, Y. J. 2007. An improved in vitro model of human intestinal follicle-associated epithelium to study nanoparticle transport by M cells. *Eur J Pharm Sci,* 30**,** 380-91.

DES RIEUX, A., RAGNARSSON, E. G., GULLBERG, E., PREAT, V., SCHNEIDER, Y. J. & ARTURSSON, P. 2005. Transport of nanoparticles across an in vitro model of the human intestinal follicle associated epithelium. *Eur J Pharm Sci,* 25**,** 455-65.

EFSA 2011. Statement of EFSA on the Evaluation of a new study related to the bioavailability of aluminium in food. *EFSA Journal 2011;9(5):2157 [16 pp.]. doi:10.2903/j.efsa.2011.2157*.

EL HAGE CHAHINE, J. M., HEMADI, M. & HA-DUONG, N. T. 2012. Uptake and release of metal ions by transferrin and interaction with receptor 1. *Biochim Biophys Acta,* 1820**,** 334-47.

EXLEY, C. 2003. A biogeochemical cycle for aluminium? *J Inorg Biochem,* 97**,** 1-7.

EXLEY, C. 2016. The toxicity of aluminium in humans. *Morphologie,* 100**,** 51-5.

FELSENFELD, A. J., RODRIGUEZ, M., COLEMAN, M., ROSS, D. & LLACH, F. 1989. Desferrioxamine therapy in hemodialysis patients with aluminum-associated bone disease. *Kidney International,* 35**,** 1371-1378.

FOGH, J., FOGH, J. M. & ORFEO, T. 1977. One hundred and twenty-seven cultured human tumor cell lines producing tumors in nude mice. *J Natl Cancer Inst,* 59**,** 221-6.

FRAGA, C. G., OTEIZA, P. I., GOLUB, M. S., GERSHWIN, M. E. & KEEN, C. L. 1990. Effects of aluminum on brain lipid peroxidation. *Toxicol Lett,* 51**,** 213-9.

FROMENT, D. H., BUDDINGTON, B., MILLER, N. L. & ALFREY, A. C. 1989a. Effect of solubility on the gastrointestinal absorption of aluminum from various aluminum compounds in the rat. *J Lab Clin Med,* 114**,** 237-42.

FROMENT, D. P., MOLITORIS, B. A., BUDDINGTON, B., MILLER, N. & ALFREY, A. C. 1989b. Site and mechanism of enhanced gastrointestinal absorption of aluminum by citrate. *Kidney Int,* 36**,** 978-84.

GULLBERG, E., LEONARD, M., KARLSSON, J., HOPKINS, A. M., BRAYDEN, D., BAIRD, A. W. & ARTURSSON, P. 2000. Expression of specific markers and particle transport in a new human intestinal M-cell model. *Biochem Biophys Res Commun,* 279**,** 808-13.

GUTTERIDGE, J. M., QUINLAN, G. J., CLARK, I. & HALLIWELL, B. 1985. Aluminium salts accelerate peroxidation of membrane lipids stimulated by iron salts. *Biochim Biophys Acta,* 835**,** 441-7.

HAASE, A., ARLINGHAUS, H. F., TENTSCHERT, J., JUNGNICKEL, H., GRAF, P., MANTION, A., DRAUDE, F., GALLA, S., PLENDL, J., GOETZ, M. E., MASIC, A., MEIER, W., THUNEMANN, A. F., TAUBERT, A. & LUCH, A. 2011. Application of laser postionization secondary neutral mass spectrometry/time-of-flight secondary ion mass spectrometry in nanotoxicology: visualization of nanosilver in human macrophages and cellular responses. *ACS Nano,* 5**,** 3059-68.

HAASE, H., HEBEL, S., ENGELHARDT, G. & RINK, L. 2015. The biochemical effects of extracellular Zn(2+) and other metal ions are severely affected by their speciation in cell culture media. *Metallomics,* 7**,** 102-11.

HANSEN, U. & THÜNEMANN, A. F. 2015. Characterization of Silver Nanoparticles in Cell Culture Medium Containing Fetal Bovine Serum. *Langmuir,* 31**,** 6842-52.

HASANOGLU, E., ALTAN, N., SINDEL, S., ONGUN, C. O., BALI, M. & ALTINTAS, E. 1994. The relationship between erythrocyte superoxide dismutase activity and plasma levels of some trace elements (Al, Cu, Zn) of dialysis patients. *Gen Pharmacol,* 25**,** 107-10.

HSIAO, I. L., HSIEH, Y. K., WANG, C. F., CHEN, I. C. & HUANG, Y. J. 2015. Trojan-horse mechanism in the cellular uptake of silver nanoparticles verified by direct intra- and extracellular silver speciation analysis. *Environ Sci Technol,* 49**,** 3813-21.

JE, H. J., KIM, E. S., LEE, J.-S. & LEE, H. G. 2017. Release properties and cellular uptake in Caco-2 cells of size-controlled chitosan nanoparticles. *Journal of Agricultural and Food Chemistry*.

JULING, S., BACHLER, G., VON GOTZ, N., LICHTENSTEIN, D., BOHMERT, L., NIEDZWIECKA, A., SELVE, S., BRAEUNING, A. & LAMPEN, A. 2016. In vivo distribution of nanosilver in the rat: The role of ions and de novo-formed secondary particles. *Food Chem Toxicol,* 97**,** 327-335.

JUNGNICKEL, H., JONES, E. A., LOCKYER, N. P., OLIVER, S. G., STEPHENS, G. M. & VICKERMAN, J. C. 2005. Application of TOF-SIMS with chemometrics to discriminate between four different yeast strains from the species Candida glabrata and Saccharomyces cerevisiae. *Anal Chem,* 77**,** 1740-5.

KÄSTNER, C. & THÜNEMANN, A. F. 2016. Catalytic Reduction of 4-Nitrophenol Using Silver Nanoparticles with Adjustable Activity. *Langmuir,* 32**,** 7383-91.

KONG, S., LIOCHEV, S. & FRIDOVICH, I. 1992. Aluminum(III) facilitates the oxidation of NADH by the superoxide anion. *Free Radic Biol Med,* 13**,** 79-81.

KRAUSE, B., MEYER, T., SIEG, H., KASTNER, C., REICHARDT, P., TENTSCHERT, J., JUNGNICKEL, H., ESTRELA-LOPIS, I., BUREL, A., CHEVANCE, S., GAUFFRE, F., JALILI, P., MEIJER, J., BOHMERT, L., BRAEUNING, A., THUNEMANN, A. F., EMMERLING, F., FESSARD, V., LAUX, P., LAMPEN, A. & LUCH, A. 2018. Characterization of aluminum, aluminum oxide and titanium dioxide nanomaterials using a combination of methods for particle surface and size analysis. *RSC Advances,* 8**,** 14377-14388.

KREWSKI, D., YOKEL, R. A., NIEBOER, E., BORCHELT, D., COHEN, J., HARRY, J., KACEW, S., LINDSAY, J., MAHFOUZ, A. M. & RONDEAU, V. 2007. Human health risk assessment for aluminium, aluminium oxide, and aluminium hydroxide. *J Toxicol Environ Health B Crit Rev,* 10 Suppl 1**,** 1-269.

KUMAR, V., BAL, A. & GILL, K. D. 2009. Aluminium-induced oxidative DNA damage recognition and cell-cycle disruption in different regions of rat brain. *Toxicology,* 264**,** 137-44.

LAMPEN, A., EBERT, B., STUMKAT, L., JACOB, J. & SEIDEL, A. 2004. Induction of gene expression of xenobiotic metabolism enzymes and ABC-transport proteins by PAH and a reconstituted PAH mixture in human Caco-2 cells. *Biochim Biophys Acta,* 1681**,** 38-46.

LEHMANN, C., SIEG, H., LAMPEN, A. & BRAEUNING, A. 2016. A. Lampen, A.Braeuning, Disturbance of firefly luciferase-based bioassays by different aluminum species, . *Anal Biochem,* 504**,** 27-9.

LESUFFLEUR, T., BARBAT, A., DUSSAULX, E. & ZWEIBAUM, A. 1990. Growth adaptation to methotrexate of HT-29 human colon carcinoma cells is associated with their ability to differentiate into columnar absorptive and mucus-secreting cells. *Cancer Res,* 50**,** 6334-43.

LEWIS, J. G. & ANDRE, C. M. 1981. Enhancement of human monocyte phagocytic function by alpha 2HS glycoprotein. *Immunology,* 42**,** 481-7.

LICHTENSTEIN, D., EBMEYER, J., KNAPPE, P., JULING, S., BOHMERT, L., SELVE, S., NIEMANN, B., BRAEUNING, A., THUNEMANN, A. F. & LAMPEN, A. 2015. Impact of food components during in vitro digestion of silver nanoparticles on cellular uptake and cytotoxicity in intestinal cells. *Biol Chem,* 396**,** 1255-64.

LICHTENSTEIN, D., EBMEYER, J., MEYER, T., BEHR, A. C., KASTNER, C., BOHMERT, L., JULING, S., NIEMANN, B., FAHRENSON, C., SELVE, S., THUNEMANN, A. F., MEIJER, J., ESTRELA-LOPIS, I., BRAEUNING, A. & LAMPEN, A. 2016. It takes more than a coating to get nanoparticles through the intestinal barrier in vitro. *Eur J Pharm Biopharm*.

LICHTENSTEIN, D., MEYER, T., BOHMERT, L., JULING, S., FAHRENSON, C., SELVE, S., THUNEMANN, A., MEIJER, J., ESTRELA-LOPIS, I., BRAEUNING, A. & LAMPEN, A. 2017. Dosimetric Quantification of Coating-Related Uptake of Silver Nanoparticles. *Langmuir,* 33**,** 13087-13097.

LIDSKY, T. I. 2014. Is the Aluminum Hypothesis Dead? *Journal of Occupational and Environmental Medicine,* 56**,** S73-S79.

LIN, C. Y., HSIAO, W. C., HUANG, C. J., KAO, C. F. & HSU, G. S. 2013. Heme oxygenase-1 induction by the ROS-JNK pathway plays a role in aluminum-induced anemia. *J Inorg Biochem,* 128**,** 221-8.

LIN, I. C., LIANG, M., LIU, T. Y., MONTEIRO, M. J. & TOTH, I. 2012. Cellular transport pathways of polymer coated gold nanoparticles. *Nanomedicine,* 8**,** 8-11.

LIUKKONEN-LILJA, H. & PIEPPONEN, S. 1992. Leaching of aluminium from aluminium dishes and packages. *Food Addit Contam,* 9**,** 213-23.

LOESCHNER, K., CORREIA, M., LÓPEZ CHAVES, C., ROKKJÆR, I. & SLOTH, J. J. 2017. Detection and characterisation of aluminium-containing nanoparticles in Chinese noodles by single particle ICP-MS. *Food Additives & Contaminants: Part A***,** 1-8.

LOTE, C. J. & SAUNDERS, H. 1991. Aluminium: gastrointestinal absorption and renal excretion. *Clin Sci (Lond),* 81**,** 289-95.

MARTIN, R. B. 1994. Aluminum: A Neurotoxic Product of Acid Rain. *Accounts of Chemical Research,* 27**,** 204-210.

MILLOUR, S., NOEL, L., KADAR, A., CHEKRI, R., VASTEL, C., SIROT, V., LEBLANC, J. C. & GUERIN, T. 2011. Pb, Hg, Cd, As, Sb and Al levels in foodstuffs from the 2nd French total diet study. *Food Chem,* 126**,** 1787-99.

MUJIKA, J. I., LOPEZ, X., REZABAL, E., CASTILLO, R., MARTI, S., MOLINER, V. & UGALDE, J. M. 2011. A QM/MM study of the complexes formed by aluminum and iron with serum transferrin at neutral and acidic pH. *J Inorg Biochem,* 105**,** 1446-56.

MUNDY, W. R., FREUDENRICH, T. M. & KODAVANTI, P. R. 1997. Aluminum potentiates glutamate-induced calcium accumulation and iron-induced oxygen free radical formation in primary neuronal cultures. *Mol Chem Neuropathol,* 32**,** 41-57.

OBEREMM, A., AHR, H. J., BANNASCH, P., ELLINGER-ZIEGELBAUER, H., GLUCKMANN, M., HELLMANN, J., ITTRICH, C., KOPP-SCHNEIDER, A., KRAMER, P. J., KRAUSE, E., KROGER, M., KISS, E., RICHTER-REICHHELM, H. B., SCHOLZ, G., SEEMANN, K., WEIMER, M. & GUNDERT-REMY, U. 2009. Toxicogenomic analysis of N-nitrosomorpholine induced changes in rat liver: comparison of genomic and proteomic responses and anchoring to histopathological parameters. *Toxicol Appl Pharmacol,* 241**,** 230-45.

OBEREMM, A., HANSEN, U., BOHMERT, L., MECKERT, C., BRAEUNING, A., THUNEMANN, A. F. & LAMPEN, A. 2016. Proteomic responses of human intestinal Caco-2 cells exposed to silver nanoparticles and ionic silver. *J Appl Toxicol,* 36**,** 404-13.

PERCY, M. E., KRUCK, T. P., POGUE, A. I. & LUKIW, W. J. 2011. Towards the prevention of potential aluminum toxic effects and an effective treatment for Alzheimer's disease. *J Inorg Biochem,* 105**,** 1505-12.

POWELL, J. J. & THOMPSON, R. P. 1993. The chemistry of aluminium in the gastrointestinal lumen and its uptake and absorption. *Proc Nutr Soc,* 52**,** 241-53.

ROLFS, A. & HEDIGER, M. A. 1999. Metal ion transporters in mammals: structure, function and pathological implications. *J Physiol,* 518**,** 1-12.

SAVORY, J., HERMAN, M. M. & GHRIBI, O. 2003. Intracellular mechanisms underlying aluminum-induced apoptosis in rabbit brain. *J Inorg Biochem,* 97**,** 151-4.

SCHÖNHOLZER, K. W., SUTTON, R. A., WALKER, V. R., SOSSI, V., SCHULZER, M., ORVIG, C., VENCZEL, E., JOHNSON, R. R., VETTERLI, D., DITTRICH-HANNEN, B., KUBIK, P. & SUTER, M. 1997. Intestinal absorption of trace amounts of aluminium in rats studied with 26aluminium and accelerator mass spectrometry. *Clin Sci (Lond),* 92**,** 379-83.

SEMISCH, A., OHLE, J., WITT, B. & HARTWIG, A. 2014. Cytotoxicity and genotoxicity of nano - and microparticulate copper oxide: role of solubility and intracellular bioavailability. *Part Fibre Toxicol,* 11**,** 10.

SIEG, H., KÄSTNER, C., KRAUSE, B., MEYER, T., BUREL, A., BÖHMERT, L., LICHTENSTEIN, D., JUNGNICKEL, H., TENTSCHERT, J., LAUX, P., BRAEUNING, A., ESTRELA-LOPIS, I., GAUFFRE, F., FESSARD, V., MEIJER, J., LUCH, A., THÜNEMANN, A. F. & LAMPEN, A. 2017. Impact of an Artificial Digestion Procedure on Aluminum-Containing Nanomaterials. *Langmuir,* 33**,** 10726-10735.

STAHL, T., TASCHAN, H. & BRUNN, H. 2011. Aluminium content of selected foods and food products. *Environmental Sciences Europe,* 23**,** 37.

TENTSCHERT, J., DRAUDE, F., JUNGNICKEL, H., HAASE, A., MANTION, A., GALLA, S., THÜNEMANN, A. F., TAUBERT, A., LUCH, A. & ARLINGHAUS, H. F. 2013. TOF-SIMS analysis of cell membrane changes in functional impaired human macrophages upon nanosilver treatment. *Surface and Interface Analysis,* 45**,** 483-485.

THOMPSON, C. E., JUNGNICKEL, H., LOCKYER, N. P., STEPHENS, G. M. & VICKERMAN, J. C. 2004. ToF-SIMS studies as a tool to discriminate between spores and vegetative cells of bacteria. *Applied Surface Science,* 231-232**,** 420-423.

VAN OOSTDAM, J. C., ZWANENBURG, H. & HARRISON, J. R. 1990. Canadian perspectives on aluminum. *Environ Geochem Health,* 12**,** 71-4.

VERISSIMO, J., GOMES, O. & GOMES, M. 2006. Leaching of aluminum from cooking pans and food containers. *Sensor Actuator B,* 118.

VICK, K. E. & JOHNSON, C. A. 1985. Aluminum-related osteomalacia in renal-failure patients. *Clin Pharm,* 4**,** 434-9.

VOLKHEIMER, G. 1974. Passage of particles through the wall of the gastrointestinal tract. *Environ Health Perspect,* 9**,** 215-25.

WAGNER, W. 1999. *Canadian Minerals Yearbook. Ottawa: Natural Resources Canada*.

WAHEED, A., BRITTON, R. S., GRUBB, J. H., SLY, W. S. & FLEMING, R. E. 2008. HFE association with transferrin receptor 2 increases cellular uptake of transferrin-bound iron. *Arch Biochem Biophys,* 474**,** 193-7.

WALCZAK, A. P., KRAMER, E., HENDRIKSEN, P. J., TROMP, P., HELSPER, J. P., VAN DER ZANDE, M., RIETJENS, I. M. & BOUWMEESTER, H. 2015. Translocation of differently sized and charged polystyrene nanoparticles in in vitro intestinal cell models of increasing complexity. *Nanotoxicology,* 9**,** 453-61.

WALTON, J. R. 2014. Chronic aluminum intake causes Alzheimer's disease: applying Sir Austin Bradford Hill's causality criteria. *J Alzheimers Dis,* 40**,** 765-838.

WEN, Z., LI, G., LIN, D. H., WANG, J. T., QIN, L. F. & GUO, G. P. 2013. [Transport of PLGA nanoparticles across Caco-2/HT29-MTX co-cultured cells]. *Yao Xue Xue Bao,* 48**,** 1829-35.

WILLHITE, C. C., BALL, G. L. & MCLELLAN, C. J. 2012. Total allowable concentrations of monomeric inorganic aluminum and hydrated aluminum silicates in drinking water. *Crit Rev Toxicol,* 42**,** 358-442.

WILLHITE, C. C., KARYAKINA, N. A., YOKEL, R. A., YENUGADHATI, N., WISNIEWSKI, T. M., ARNOLD, I. M., MOMOLI, F. & KREWSKI, D. 2014. Systematic review of potential health risks posed by pharmaceutical, occupational and consumer exposures to metallic and nanoscale aluminum, aluminum oxides, aluminum hydroxide and its soluble salts. *Crit Rev Toxicol,* 44 Suppl 4**,** 1-80.

XIA, D., HE, Y., LI, Q., HU, C., HUANG, W., ZHANG, Y., WAN, F., WANG, C. & GAN, Y. 2017. Transport mechanism of lipid covered saquinavir pure drug nanoparticles in intestinal epithelium. *J Control Release,* 269**,** 159-170.

YANG, S., DAMIANO, M. G., ZHANG, H., TRIPATHY, S., LUTHI, A. J., RINK, J. S., UGOLKOV, A. V., SINGH, A. T., DAVE, S. S., GORDON, L. I. & THAXTON, C. S. 2013. Biomimetic, synthetic HDL nanostructures for lymphoma. *Proc Natl Acad Sci U S A,* 110**,** 2511-6.

YE, D., BRAMINI, M., HRISTOV, D. R., WAN, S., SALVATI, A., ABERG, C. & DAWSON, K. A. 2017. Low uptake of silica nanoparticles in Caco-2 intestinal epithelial barriers. *Beilstein J Nanotechnol,* 8**,** 1396-1406.

YOKEL, R. A. & MCNAMARA, P. J. 1988. Influence of renal impairment, chemical form, and serum protein binding on intravenous and oral aluminum kinetics in the rabbit. *Toxicol Appl Pharmacol,* 95**,** 32-43.

YOKEL, R. A. & MCNAMARA, P. J. 2001. Aluminium toxicokinetics: an updated minireview. *Pharmacol Toxicol,* 88**,** 159-67.

YOKEL, R. A., URBAS, A. A., LODDER, R. A., SELEGUE, J. P. & FLORENCE, R. L. 2005. 26Al-containing acidic and basic sodium aluminum phosphate preparation and use in studies of oral aluminum bioavailability from foods utilizing 26Al as an aluminum tracer. *Nuclear Instruments and Methods in Physics Research Section B: Beam Interactions with Materials and Atoms,* 229**,** 471-478.

ZATTA, P., KISS, T., SUWALSKY, M. & BERTHON, G. 2002. Aluminium(III) as a promoter of cellular oxidation. *Coordination Chemistry Reviews,* 228**,** 271-284.

ZHANG, Q. L., LI, M. Q., JI, J. W., GAO, F. P., BAI, R., CHEN, C. Y., WANG, Z. W., ZHANG, C. & NIU, Q. 2011. In vivo toxicity of nano-alumina on mice neurobehavioral profiles and the potential mechanisms. *Int J Immunopathol Pharmacol,* 24**,** 23s-29s.

ZHOU, Y. & YOKEL, R. A. 2005. The chemical species of aluminum influences its paracellular flux across and uptake into Caco-2 cells, a model of gastrointestinal absorption. *Toxicol Sci,* 87**,** 15-26.